TAYLOR VORTICES AND BENARD CELLS: THE EMERGENT COMPLEXITY OF TWO SIMPLE FLUID SYSTEMS

By

James M. Thomson

Submitted in partial fulfillment of
the requirements for the degree of
Bachelor of Arts
Department of Physics
Middlebury College
Middlebury, Vermont

May 2000

ABSTRACT

This thesis is a theoretical and experimental examination of the formation of complex, patterned flow in two simple fluid systems. Taylor vortices form in the annulus between rotating, concentric cylinders (in our case: inner rotating, outer stationary). Taylor vortices were observed experimentally and the onset of these vortices was shown to behave in accordance with theory. By varying the spacing between the cylinders and fluid properties, such as viscosity, it was possible to demonstrate the fundamental properties of this phenomena. Benard cells are convective cells that form when a thin layer of fluid is heated from below. The investigation of Benard cells in this thesis was not as thorough as for the Taylor vortices, but the experiments still demonstrated the dynamical similarities between the Benard and Taylor systems. These systems are discussed as ideal models or paradigms for understanding the spontaneous emergence of complexity.

Advisor: _____

Jeffery S. Dunham

Commitee: _____

_____

Date Accepted: _____

To my parents,

who have always believed in me and who taught me to do the same...

"You're going to find, Luke, that many of the truths we cling to depend upon a certain point of view."

-Obi Wan

ACKNOWLEDGMENTS

I would like to thank my family for the constant encouragement and humor. Dad, you have taught me to work hard and take pride in what I do. Mom, you have taught me to learn at every opportunity and to think critically about the world around me. Heather, thanks for making me laugh and enjoy reality (or my perception there of).

Jess, without your patience and support I am not sure what I would do. Thank you for the smiles.

My advisor, Jeff Dunham, you have been a constant source of inspiration since my first day in your classroom. You have forever altered and widened my view of the physical world. Thank you for the wisdom and humor (and breakfast at Steve's Diner).

Crispin Butler, your constant willingness to help with experiments and push me further with questions I did not know how to answer has made this the most intensive learning process of my life. There are few people so dedicated to education.

To Charlie and Tony, thanks for all the patient hours in the machine shop. I would not have known where to begin.

To all my fellow Varsity Physics '00 survivors, I could not have made it through without you. Anybody want to do one more problem set...just for fun?

To the Middlebury Men's Crew Team, the Middlebury Ski Patrol, and the Fahm House Boys, thanks for all the visits to the 5th floor. It's been entertaining.

CONTENTS

LIST OF FIGURES

B.

LIST OF TABLES

LIST OF SYMBOLS

Quantity	Symbol	Unit
angular speed	Ω	rad s^{-1}
cylinder radius	a_n	cm
mass density	ρ	g cm^{-3}
velocity vector field	$\boldsymbol{u}$	cm/s
viscosity	μ	cp = g cm^{-1} s^{-1} x 10^{-2}
kinematic viscosity	ν	cS = cm^2 s^{-1} x 10^{-2}
time	t	s
pressure	p	g cm^{-1} s^{-2}
Reynolds number	Re	dimensionless
acceleration due to gravity	g	m s^{-2}
uncertainty in x	σ_x	$[x]$
temperature	T	°C
volume coefficient of expansion	α	$°C^{-1}$
thermal diffusivity	κ	cm^2 s^{-1}
gap between boundaries	d	cm
Rayleigh number	Ra	dimensionless
surface tension coefficient	S	s^{-2}
Marangoni number	Ma	dimensionless

Chapter I
Introduction

1.1 Description of Taylor-Couette flow and Benard convection

This thesis will examine the emergence of complex, organized behavior in two simple fluid systems: Taylor-Couette flow and Benard convection. The goal will be to understand when and how the complex behavior emerges, and to verify this understanding experimentally. Each system is defined by driving forces and dissipative forces. The driving forces produce motion, while the dissipative forces work to restrain, oppose, and dampen this motion. The complex flows of Taylor vortices and Benard cells occur after reaching the critical point at which the driving forces begin to overpower the dissipative forces.

In the Taylor-Couette flow, fluid is contained in the annulus between two concentric cylinders, and the inner cylinder is rotated (see Fig. 1.1a). This rotation produces a centrifugal driving force that moves fluid radially outward. The motion is resisted by the dissipative force of the viscosity of the fluid (friction due to relative movement of fluid particles). Once the inner cylinder is rotated fast enough, the centrifugal forces win and the system makes a transition from *laminar* (simple) flow to complex rolling toroidal vortices, called *Taylor vortices* (shown in Fig. 1.1b). The focus of this thesis is the critical point at which this complexity emerges and the experimental determination of the properties of the critical point with an uncertainty of only a few percent. A limited investigation was also made of the complex flows that occur when the rotation rate is increased well beyond the critical point.

In the Benard convection a thin layer of fluid is heated from below as shown in Fig. 1.2a. There are two dissipative forces present: the viscosity of the fluid, and the thermal diffusivity of the fluid (heat transfer between fluid particles). The system is driven by the temperature difference between boundaries which results in either a buoyancy force or a surface tension force, depending on the experiment (discussed in

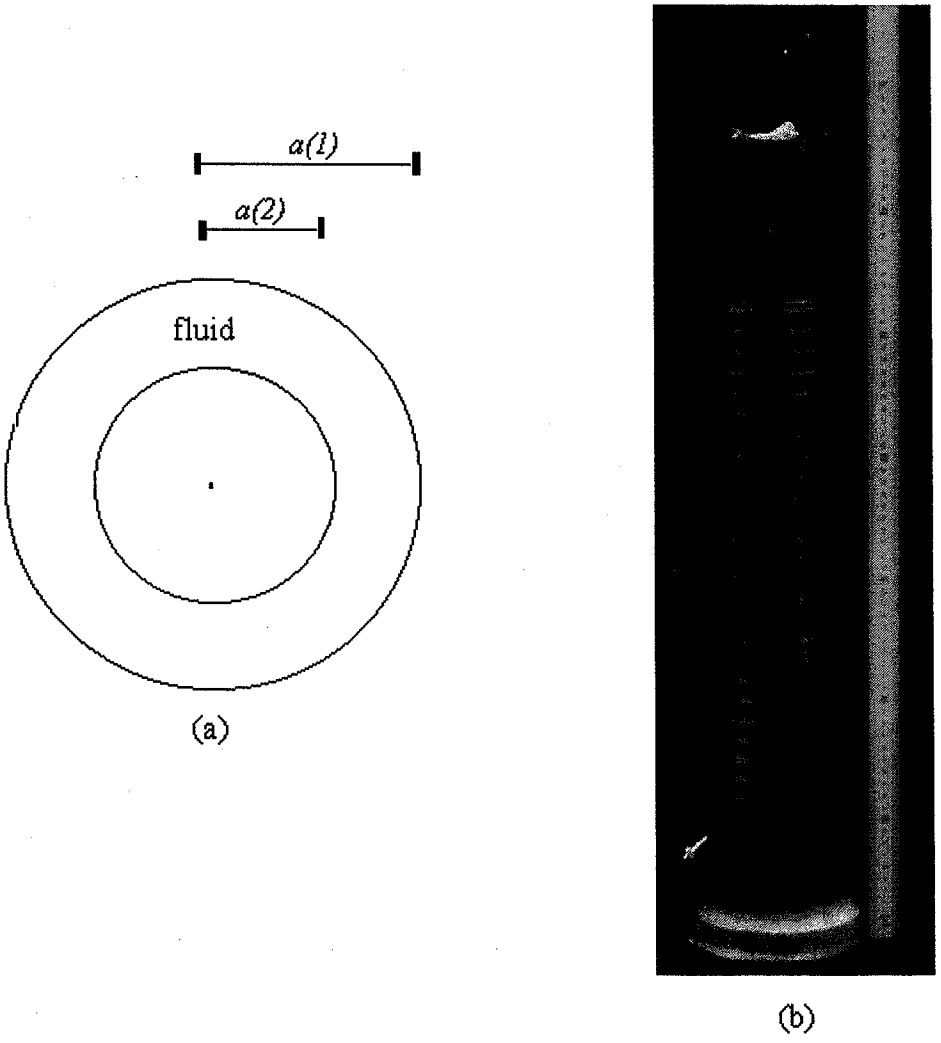

FIG. 1.1. Taylor-Couette flow: (a) cross-sectional view (top view) and (b) Taylor vortices produced in the final apparatus.

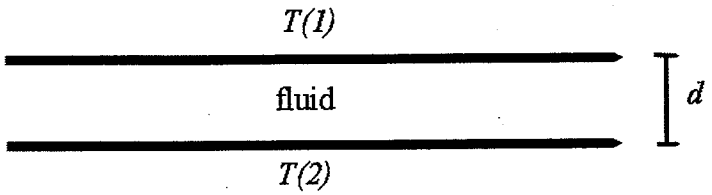

(a)

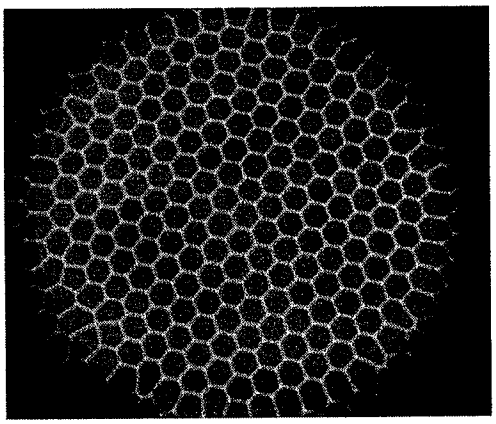

(b)

FIG. 1.2. Benard convection; (a) standard boundary conditions;
(b) hexagonal convection cells, as viewed from above (Koschmieder 1993, p. 55).

Chapter V). When this system is driven beyond the critical point, complex motion in the form of ordered convection cells arises. These *Benard cells* are shown in Fig. 1.2b and will be described fully in Section 5.2. The theory of both driving forces will be discussed briefly, but only the surface tension driven case was examined experimentally. Although these experiments were much less complete than the Taylor vortices measurements, the criticality of the onset of convection was still verified successfully. As is evident from the reviews by Koschmeider (1993) and Tagg (1992), there have been thousands of publications on the topic of Taylor vortices and Benard cells; this thesis will be restricted to the experimental verification of the fundamental theories surrounding these phenomena.

1.2 Stability and the bifurcation of states

Theoretical understanding of the emergence of complexity in these fluid systems is based on the concept of stability. A transition from stable to unstable flow occurs at the critical point at which the driving forces overpower the dissipative forces. In the stable case, the fluid behaves as expected from Newtonian mechanics and the flow is laminar. When it becomes unstable, the flow becomes extremely sensitive to small disturbances and to the geometric conditions of the experiment. When this critical point is reached and instability begins, the behavior of the system is said to *bifurcate*. As shown in Fig. 1.3, this bifurcation means that there are now two solutions for the motion of the fluid: one is stable and the other is unstable. However the unstable solution is no longer possible realistically, and the system follows the upper path of the bifurcation diagram. Following the lower path after the bifurcation point in Fig. 1.3 would be analogous to a pin resting vertically upright on its point; under absolutely ideal conditions the solution is possible, but because it is so sensitive to any small disturbance the pin will soon fall, and thereby follow the upper path.

It is important to note here that the onset of instability does not mean equilibrium no longer exists. The bifurcation of the system simply means that the stable equilibrium solution now has a more complex structure; the laminar equilibrium solution continues to

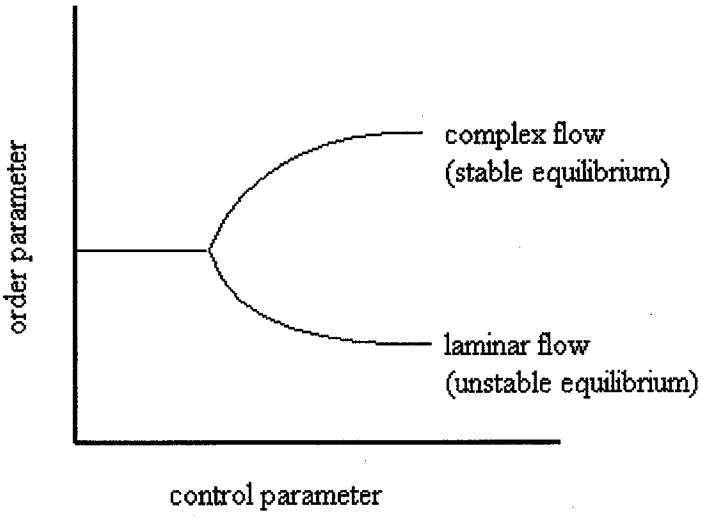

FIG. 1.3. Bifurcation of states diagram. Branching of path coresponds to the emergence of complexity.

exist, but the likelihood that it would ever be seen experimentally is vanishingly small because it is unstable. The bifurcation paradigm is often used to describe complex systems; Taylor vortices and Benard cells are an ideal illustration of the concept.

1.3 Implications of emergent complexity

The emergence of Taylor vortices and Benard cells in simple fluid systems provides an ideal introduction to the study of complexity. These phenomena represent the emergence of complex patterns and flows in fluid systems whose motions are predicted to be simple, or *laminar*, by convention mechanics. Consistent with the current understanding of complexity, the emergence of Taylor vortices and Benard cells demonstrates the concepts of criticality, phase transitions, scale independence, and sensitivity to initial conditions. Despite very few experimental similarities, Taylor vortices and Benard cells follow precisely the same model for the evolution of complex flows and patterns. I believe it is worthwhile to consider the emergent complexity of these two systems in a much broader context. Certainly the analysis of these two fluid systems does not presume to explain all of the mysteries of the world around us; yet I believe these phenomena to be significant to the entire scientific community.

There has a been a dramatic shift in scientific thinking over the past forty years. Researchers and theorists from all disciplines have begun to look beyond reductionist models of fundamental particles and components; these scientists are now studying systems and their emergent behavior. In the past, science has been defined by the search for simple, universal laws to describe and predict the universe. This search is no longer adequate. As part of this philosophical shift in scientific thinking, it has been demonstrated in chaos theory that simple, fully deterministic conditions do not necessarily result in predictable, simple behavior. In fact, simple behavior is often the exceptional case, and complexity far better describes the majority of phenomena in the world around us. Efforts to understand how complexity arises and functions are currently underway in all disciplines. The applications of these ideas are vast: How does the complexity of global weather patterns arise from gas and liquid particle motion? How

does intelligent life arise from individual cells and tissues? How does an intricate global economy arise from the simple exchange of goods, services, and information between self-interested individuals? These are questions that can only be tackled by a study of systems and of complexity itself, not the individual components alone.

Taylor vortices Benard cells represent order and organization that is unexpected by the laws of mechanics, especially the second law of thermodynamics, and this leads us to wonder from whence the complexity arises. Perhaps the whole system is capable of behavior that cannot be explained in principle by summing the action of a nearly infinite number of fluid particles. We may further ask: should this be so wondrous and unexpected, this spontaneous emergence of complexity? Perhaps, as Stuart Kauffman (1995) suggests, complexity spontaneously arising from simple constituents is exactly what we should expect, and the very existence of intelligent life is inevitable in a system such as this universe. As we move forward into a more thorough and less philosophical discussion of the emergent complexity of Taylor vortices and Benard cells, I ask the reader to keep in mind the ideas above and the possibilities for an increased understanding of the complexity that constantly surrounds us and *is* us.

Chapter II

Taylor-Couette flow: history and theory

2.1 History

The Taylor-Couette flow has been the subject of constant investigation during the twentieth century, and the idea of concentric rotating cylinders containing fluid in the annulus between them has been around for nearly 300 years (Donnelly 1991, p. 33). The first known reference to such a fluid system is found in Issac Newton's *Principia*. In Book II, Section IX, Newton defined what we know today as a Newtonian fluid, where the viscous stresses (the friction between fluid particles) are in proportion to the velocity gradient. He discussed such a fluid contained between two rotating cylinders:

> If a fluid be contained in a cylindric vessel of an infinite length, and contain another cylinder within, and both the cylinders revolve about one common axis, and times of their revolutions be as their semidiameters, and every part of the fluid continues in its motion, the periodic times of the several parts will be as the distances from the axis of the cylinders (Newton, p. 385).

Here Newton described what we know today as *laminar* flow in a Taylor-Couette apparatus. It is unlikely that Newton could envision the complexity that would emerge in this system. However, Newton did recognize the intrinsic simplicity and symmetry of such a flow, presumably with the intuition that it would be worth studying.

George Stokes, one of the most important contributors to the development of theoretical fluid dynamics, took the next step in the development of the concentric cylinder model. In 1848 he published a paper in which he presented a mathematical description of the velocity of the fluid between two cylinders revolving at different angular velocities. He also made the insightful statement that, "if the inner [cylinder] were made to rotate too fast, the fluid near it would have a tendency to fly outwards in consequence of the centrifugal force, and eddies would be produced (Stokes 1888, p. 102)." Stokes's understanding that the rotation of the inner cylinder would result in instabilities was not seen experimentally until the work of G. I. Taylor in the 1920's

(Donnelly 1991, p. 33). During the 75 years between Stoke's paper and Taylor's work, the rotating cylinder system was studied primarily as a method of measuring viscosity, and usually only the outer cylinder was rotated.

Working independently of each other, Arnulph Mallock and M. Maurice Couette built and studied rotating cylinder *viscometers* during the late nineteenth century, and it seems to be a historical accident that only Couette's name is associated with the flow. Both researchers measured the torque on the inner cylinder when the outer was rotated and used this torque to determine the viscosity of the fluid in the annulus between the cylinders. Mallock experimented with rotating the inner cylinder, and he concluded from his experiments that this flow would *always* be unstable (Donnelly 1991, p. 35). This incorrect conclusion from his experiments was due to the fact that he set the angular velocity of his inner cylinder above the critical value to amplify instabilities (to be discussed later). Couette published his thesis on viscosity in 1890 and in it he stated that the viscosity of water appeared constant until a critical angular velocity was achieved by the inner cylinder (Couette 1890, p. 433). Thus, early experimental work with rotating cylinder systems had begun to discover the instabilities associated with the rotation of the inner cylinder, but the ground work for understanding this phenomena would not be in place until a 1923 paper by G. I. Taylor (Donnelly 1991, p. 36).

Taylor applied *linear stability theory* to the rotating cylinder flow, and he conducted the first thorough experimental study of the patterns, or *Taylor vorticies,* that occur above a critical angular velocity of the inner cylinder. He dropped ink in to the fluid to aid visualization, and this made the sharp onset of the patterns far more evident than anything seen with a viscometer apparatus. The theory Taylor developed predicted that the fluid would change from smooth, or *laminar*, flow into distinct patterns (Taylor 1923, p. 289). This paper prompted further study of rotating cylinder systems, and the flow soon became known as the Taylor-Couette flow.

The Taylor-Couette flow was then analyzed further in the 1950s by S. Chandrasekhar. Chandrasekhar generalized Taylor's theory and inspired more experimental work on various flow phenomena. In 1965, work by D. Coles showed the development of Taylor vorticies to be universal across a wide range of geometric scale

(Donnelly 1991, p. 38). The study of the Taylor-Couette flow has continued to the present day, and, as discussed in a recent book by E. L. Koschmieder (1993), research has become so extensive that it is difficult to keep track of the numerous publications. Perhaps the most interesting area of recent research has been the study of the turbulence (chaotic flow) that evolves from the Taylor vortices at extreme rotation rates.

2.2 Navier-Stokes equation and equations of motion

The Navier-Stokes equation is the fundamental dynamical equation for a fluid of constant density; the equation expresses Newton's second law of motion by relating the forces present in a dynamic fluid to the inertia of the fluid. To derive the Navier-Stokes equation, we must assume that the hypothesis of continuum mechanics applies to fluid particles. This means that we can measure and use macroscopic quantities that are the result of averaging over a large number of molecules and that these properties will be continuous through the fluid (Tritton 1988, p. 48). The two properties that we are primarily concerned with are the velocity $\boldsymbol{u}(r,t)$ of the flow and the mass density of the flow $\rho(r,t)$, which are both functions of time and position. We must also require the law of mass conservation given by the *continuity equation*

$$\frac{\partial \rho}{\partial t} + \nabla \cdot (\rho \, \mathbf{u}) = 0 \tag{2.1}$$

(Tritton 1988, p. 52). For duration of this chapter and our discussion of the Taylor-Couette flow, we will be concerned only with fluids of constant density ρ. Thus, Eq. 2.1 reduces to

$$\nabla \cdot \boldsymbol{u} = 0. \tag{2.2}$$

Next we need to develop Newton's second law by expressing the rate of change of linear momentum in a fluid particle as equal to the net force acting on it. The subtlety here is that we cannot simply equate the rate of change of momentum at a fixed point to the force, because different particles will be at that point at different times. The particles are subject to the laws of mechanics, not the points in space, and so we must follow these particles over small amounts of time *dt*. We need to know the rate of change of a quantity

as we follow a fluid particle, and express this rate in terms of other quantities that refer to fixed points in space. The change dQ in a quantity Q of a given fluid particle will have two parts: the change $(\partial Q/\partial t)dt$ due to a change in time dt while at a fixed point in space, and the change $\nabla Q \cdot d\boldsymbol{r}$ due to a change in space $d\boldsymbol{r}$ while at a fixed point in time, as shown in Fig. 2.1 (Symon 1971, p. 313). Dividing dQ by dt to achieve an expression for the rate, gives us

$$\frac{dQ}{dt} = \frac{\partial Q}{\partial t} + (\nabla Q) \cdot \left(\frac{d\boldsymbol{r}}{dt} \right), \tag{2.3}$$

which can also be written in terms of the velocity vector field $\boldsymbol{u}(\boldsymbol{r},t)$

$$\frac{dQ}{dt} = \frac{\partial Q}{\partial t} + \boldsymbol{u} \cdot (\nabla Q). \tag{2.4}$$

This time derivative is called the *substantive derivative*[1] and is usually denoted by $\frac{DQ}{Dt}$.

For vector functions it is expressed by the operator

$$\frac{\mathrm{D}}{\mathrm{D}t} = \frac{\partial}{\partial t} + \boldsymbol{u} \cdot \nabla \tag{2.5}$$

(Landau and Lifshitz 1987, p. 3). Thus, the rate of change of velocity measured by a particle co-moving with the fluid is

$$\frac{\mathrm{D}\mathbf{u}}{\mathrm{D}t} = \frac{\partial \mathbf{u}}{\partial t} + (\mathbf{u} \cdot \nabla)\mathbf{u}. \tag{2.6}$$

Returning to our goal of deriving the dynamical equation for constant density fluid flow, multiplying Eq. 2.4 by the density ρ gives the rate of change of linear momentum per unit volume when following a particle co-moving with the fluid

$$\rho \frac{\mathrm{D}\mathbf{u}}{\mathrm{D}t} = \rho \frac{\partial \mathbf{u}}{\partial t} + \rho\, (\mathbf{u} \cdot \nabla)\mathbf{u}. \tag{2.7}$$

(The density ρ remains outside of the operator because it is constant.) According to Newton's second law, the right-hand side of Eq. 2.5 should equal the net force per unit volume acting on the fluid particle we are following. The three possible forces are the pressure force, the viscous force, and any external force, e.g. gravity.

---

[1] In using the term *substantive derivative*, we've followed the convention of Tritton's text, *Physical Fluid Dynamics*. This derivative is also called the *total*, *material*, or *convective* derivative in other references.

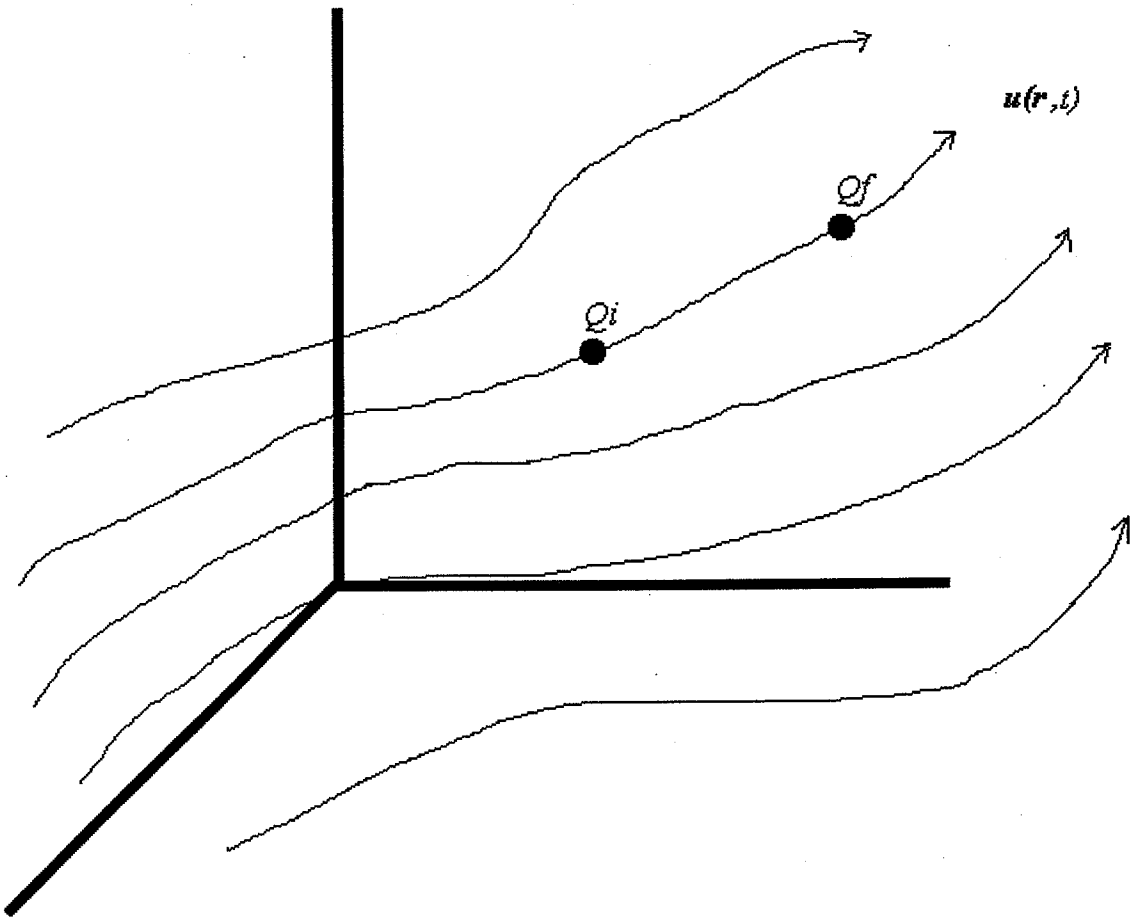

FIG. 2.1. The substantive derivative operator evaluates the change $Qf - Qi$ in a quantity $Q(\mathbf{r},t)$ while following a fluid flow defined by the velocity vector field $\mathbf{u}(\mathbf{r},t)$.

The net pressure force per unit volume is a result of a spatial change in the pressure p, so we can express the pressure contribution to the net force per unit volume by the negative gradient of p, $-\nabla p$. The viscous force per unit volume for a fluid of constant density is given by $\mu\nabla^2\boldsymbol{u}$, where μ is the coefficient of viscosity (Tritton 1988, p. 58-59). Viscous stresses oppose the relative movement of neighboring particles; we will use a two dimensional example to illustrate the origin the viscous force term. We consider a fluid with velocity u in the x direction and a simple velocity variation $u(y)$. A stress will act in the plane perpendicular to any velocity variation. This stress is directly proportional to the velocity gradient, and therefore the force per unit area τ will be given by $\mu\frac{\partial u}{\partial y}$ (Tritton 1988, p. 4). To generalize this idea we must consider velocity variations of $|\boldsymbol{u}(\boldsymbol{r})|$ in all directions and stresses possible in any plane of three-dimensional space. The result is the viscous force per unit volume $\mu\nabla^2\boldsymbol{u}$; this expression is far more complicated to envision qualitatively, yet the fundamental concept of stresses due to spatial velocity variations remains.[2] If we consider net external forces per unit volume to be $\boldsymbol{F}$, the force contributions sum to form the dynamic equation

$$\rho\frac{D\boldsymbol{u}}{Dt} = -\nabla p + \mu\nabla^2\boldsymbol{u} + \boldsymbol{F}. \tag{2.8}$$

The above is the common form of the Navier-Stokes equation, and using Eq. 2.5 we can rewrite it as

$$\rho\frac{\partial\,\mathbf{u}}{\partial\,t} + (\mathbf{u}\cdot\nabla)\mathbf{u} = -\nabla p + \mu\nabla^2\mathbf{u} + \mathbf{F}. \tag{2.9}$$

This is the non linear partial differential equation for $\boldsymbol{u}$ that governs fluid flow, and we will now apply it, subject to the continuity equation, Eq. 2.2, to the Taylor-Couette flow.

[2] A thorough mathematical derivation of the viscous force term is presented in Tritton (1988, p. 69-72).

2.3 Applying the Navier-Stokes equation

It is clear from the geometry of the Taylor-Couette flow shown in Fig. 2.2 that cylindrical polar coordinates will be the most useful for analyzing this flow. The general form of the continuity equation when expressed in cylindrical polar coordinates is

$$\frac{\partial u_r}{\partial r}+\frac{u_r}{r}+\frac{1}{r}\frac{\partial u_\phi}{\partial \phi}+\frac{\partial u_r}{\partial z}=0. \tag{2.10}$$

(Tritton 1988, p. 60). Evaluating the individual components of Eq. 2.7 in cylindrical polar coordinates is somewhat lengthy, and we will only outline the process here. There is subtlety involved because $\boldsymbol{u}(r,\phi,z,t)$ is a vector field and the basis vectors $\boldsymbol{e}_r$, $\boldsymbol{e}_\phi$, $\boldsymbol{e}_z$ of cylindrical polar coordinates are not constant relative to position. To evaluate $(\boldsymbol{u}\cdot\nabla)\boldsymbol{u}$ in the left hand side and $\nabla^2\boldsymbol{u}$ in the right hand side we must use the following two relations

$$(\boldsymbol{u}\cdot\nabla)\boldsymbol{u}=\tfrac{1}{2}\nabla(\boldsymbol{u}\cdot\boldsymbol{u})-\boldsymbol{u}\times(\nabla\times\boldsymbol{u}), \tag{2.11}$$

$$\nabla^2\boldsymbol{u}=\nabla(\nabla\cdot\boldsymbol{u})-\nabla\times(\nabla\times\boldsymbol{u}) \tag{2.12}$$

(Griffiths 1989, p. 24-27). We can then finish evaluating Eq. 2.7 using standard cylindrical polar forms of the gradient, divergence, and curl. (Griffiths 1989, p. 45). We will quote the resulting components of Eq. 2.7; the radial component of the Navier-Stokes equation in cylindrical polar coordinates becomes

$$\rho\left[\frac{\partial u_r}{\partial t}+u_r\frac{\partial u_r}{\partial r}+\frac{u_r}{r}\frac{\partial u_r}{\partial\phi}+u_z\frac{\partial u_r}{\partial z}-\frac{u_\phi^2}{r}\right]= -\frac{\partial p}{\partial r}+\mu\left[\frac{\partial^2 u_r}{\partial r^2}+\frac{1}{r}\frac{\partial u_r}{\partial r}-\frac{u_r}{r^2}+\frac{1}{r^2}\frac{\partial^2 u_r}{\partial\phi^2}+\frac{\partial^2 u_r}{\partial z^2}-\frac{2}{r^2}\frac{\partial u_\phi}{\partial\phi}\right]+F_r, \tag{2.13}$$

the azimuthal component becomes

$$\rho\left[\frac{\partial u_\phi}{\partial t}+u_r\frac{\partial u_\phi}{\partial r}+\frac{u_r u_\phi}{r}+\frac{u_\phi}{r}\frac{\partial u_\phi}{\partial\phi}+u_z\frac{\partial u_\phi}{\partial z}\right]= -\frac{1}{r}\frac{\partial p}{\partial\phi}+\mu\left[\frac{\partial^2 u_\phi}{\partial r^2}+\frac{1}{r}\frac{\partial u_\phi}{\partial r}-\frac{u_\phi}{r^2}+\frac{1}{r^2}\frac{\partial^2 u_\phi}{\partial\phi^2}+\frac{\partial^2 u_\phi}{\partial z^2}+\frac{2}{r^2}\frac{\partial u_r}{\partial\phi}\right]+F_\phi, \tag{2.14}$$

and the axial component becomes

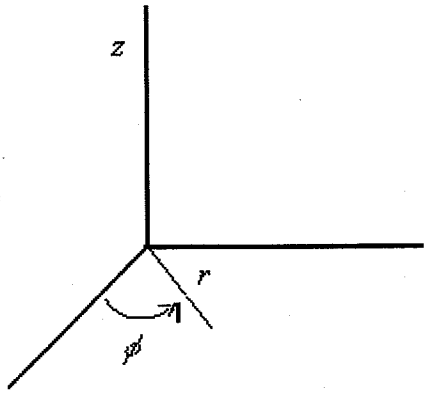

(a)

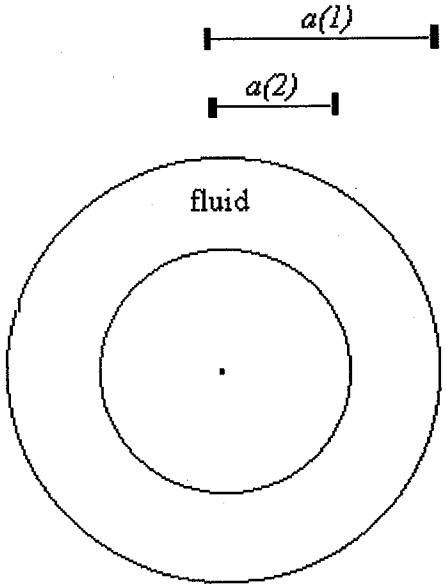

(b)

FIG. 2.2. Geometry of Taylor-Couette flow; (a) standard cylindrical polar coordinates (*z* axis corresponds to common axis of the two cylinders) and (b) top view of apparatus (z axis into the page).

$$\rho\left[\frac{\partial u_z}{\partial t}+u_r\frac{\partial u_z}{\partial r}+\frac{u_\phi}{r}\frac{\partial u_z}{\partial \phi}+u_z\frac{\partial u_z}{\partial z}\right]= \\ -\frac{\partial p}{\partial z}+\mu\left[\frac{\partial^2 u_z}{\partial r^2}+\frac{1}{r}\frac{\partial u_z}{\partial r}+\frac{1}{r^2}\frac{\partial^2 u_z}{\partial \phi^2}+\frac{\partial^2 u_z}{\partial z^2}\right]+F_z \tag{2.15}$$

(Landau and Lifshitz 1987, p. 48). We now wish to solve for the velocity distribution of laminar flow within the annulus between the cylinders for the case of the inner cylinder rotating with angular speed Ω and the outer cylinder at rest. We begin by assuming that the velocity is only in the azimuthal direction ($\boldsymbol{u} = u_\phi \mathbf{e}_\phi$), and that the velocity component u_ϕ depends solely upon the radial position r ($u_\phi = u_\phi(r)$). These assumptions apply only to laminar flow, but they form the foundation of the theoretical understanding of more complex flows. Because $\frac{\partial u_\phi}{\partial \phi}=0$, this flow will satisfy the continuity equation, Eq. 2.8, and with these assumptions we can simplify the components of the Navier-Stokes equation. Equation 2.11 does not contribute anything because $u_z = 0$. Still building from these assumptions, Eq. 2.10 for the azimuthal component of the Navier-Stokes equation becomes

$$0=\mu\left[\frac{\partial^2 u_\phi}{\partial r^2}+\frac{1}{r}\frac{\partial u_\phi}{\partial r}-\frac{u_\phi}{r^2}\right], \tag{2.16}$$

and Eq. 2.9 for the radial component of the Navier-Stokes becomes

$$-\frac{\rho u_\phi^2}{r}=-\frac{dp}{dr}. \tag{2.17}$$

As with any attempt to solve a differential equation, we must include the boundary conditions. We consider both cylinders to be impermeable walls, so $\boldsymbol{u}\cdot\boldsymbol{r} = 0$ for $r = a_1$ and $r = a_2$. We will also introduce the *no-slip* condition, which states that the fluid next to the rotating cylinder cannot have any tangential component of velocity relative to the wall, or more formally: $\boldsymbol{u} \times \boldsymbol{r} = 0$ at each wall (Tritton 1988, p. 62). These boundary conditions lead to the conclusion that

$$u_\phi = \Omega a_1 \quad \text{at} \quad r=a_1, \quad \text{and} \quad u_\phi = 0 \quad \text{at} \quad r=a_2. \tag{2.18}$$

The solution to Eq. 2.12 can be found by separating variables and integrating in terms of the variable (u_0 / r), and it is of the form

$$u_o = Ar + B/r \tag{2.19}$$

Applying the boundary conditions, we find that

$$A = -\Omega a_1^2 \Big/ (a_2^2 - a_1^2) \quad \text{and} \quad B = \Omega a_1^2 a_2^2 \Big/ (a_2^2 - a_1^2) \tag{2.20}$$

(Tritton 1988, p. 108). Thus, we have developed an expression to show the velocity distribution inside a Taylor-Couette apparatus, under the assumption of ideal laminar flow.

2.4 Instabilites and patterns in the Taylor-Couette flow

Thus far our development of the Taylor-Couette flow has been restricted to ideal laminar flow, yet this is only a small fraction of the flows seen in a Taylor-Couette system. When the flow is laminar, the viscous force dissipates the centrifugal force resulting from circular motion; with higher rotation rates, the driving force of the circular motion overpowers the viscous force, and more complex flows (with u_z and u_φ no longer zero) result. More accurately, it is the no-slip condition at the cylinder walls that provides the driving force by producing a shear stress on the fluid between the cylinders. However, we will not take the time to delve into evaluating the stress tensor; we will continue to assume that the significant result is that fluid particles will be pushed radially outward once the viscous stress has been overcome.

The transition to a complex flow in the Taylor-Couette system occurs at a precise critical point (when the driving forces overpower the dissipative forces) and is the result of instability in the flow. The linear theory of hydrodynamic stability was developed to explain and understand these instabilities. Fundamentally, stability theory states that changes from one type of flow to another are the result of spontaneously amplified disturbances present in the system. Extreme and precise *phase transitions* (i.e. the formation and/or change of patterns) will occur in the flow without an outside disturbance, and the linear theory of hydrodynamic stability determines when these amplifications will occur (Tritton 1988, p. 255).

Qualitatively, the patterns seen in a Taylor-Couette flow are the result of small vortices, or Taylor cells, that occur as toroids that surround the inner cylinder, as seen in

Fig. 2.3. We will consider a small toroidal element of fluid (contained within dr and dz) that becomes displaced to a slightly larger radius. If it now has a higher velocity than the surrounding particles, it will continue to move outward because the inward radial pressure at that position will be insufficient to balance the force of the fluid element's motion outward. Likewise, a toroidal element of fluid (again contained within dr and dz) that is shifted slightly inwards will continue to move to the interior. Thus, there is an instability for some distributions of u_ϕ. Using a simplified model with no viscous dissipation of the driving force, a toroidal element at $r = r_0$ will be displaced if its angular momentum Ωr^2 is greater than the angular momentum of the toroidal element at $r = r_0 + dr$. Thus, instability occurs if angular momentum decreases with an increase in radius r. This is expressed by the *Rayleigh criterion*

$$\frac{\mathrm{d}}{\mathrm{d}r}\left|\Omega r^2\right| < 0 \tag{2.21}$$

for instability in the Talyor-Couette flow (Tritton 1988, p. 261). As mentioned above, this discussion of instability does not include the stabilizing force of viscosity, and the full application of the linear theory of hydrodynamic stability is required to truly determine when the system will be unstable to small perturbations.

2.5 Dynamic similarity

Before applying the linear theory of hydrodynamic stability, we need to introduce the concept of *dynamic similarity*. From constructing and solving the Navier-Stokes equation, we can see that any flow can be specified by three parameters: the kinematic viscosity ν (defined as the ratio of the viscosity coefficient μ to the mass density ρ, $\nu \equiv \mu/\rho$), a velocity scale U, and a length scale L. Dynamic similarity occurs when two flows have the same ratio of velocity to the velocity scale at geometrically similar points in the system. In simple one dimensional cartesian coordinates this means that the ratio $u' = u/U$ is the same when the ratio $x' = x/L$ is the same (Tritton 1988, p. 91). We can combine these concepts to form a scale-independent and dimensionless quantity called the *Reynolds number*

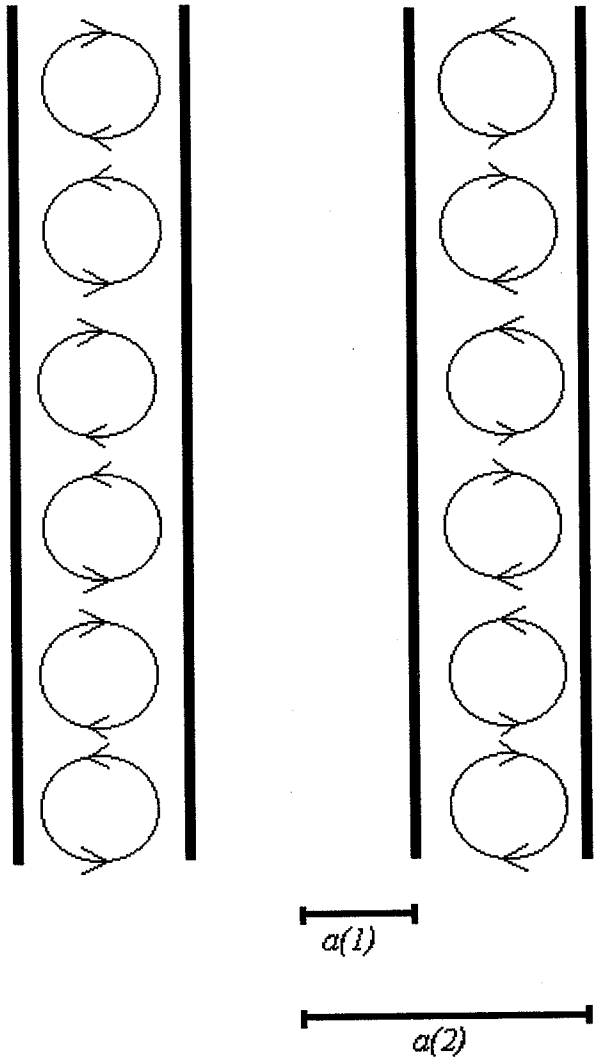

FIG. 2.3. Movement within Taylor vortices (Tritton 1988, p. 260).

$$\mathrm{Re} \equiv UL/\nu . \tag{2.22}$$

In systems that are geometrically similar, we claim dynamic similarity if the systems have the same Reynolds number (Landau and Lifshitz 1987, p. 57). For Taylor-Couette flow, the Reynolds number is defined as

$$\mathrm{Re} = \Omega a_1 (a_2 - a_1)/\nu \tag{2.23}$$

(Tritton 1988, p. 261). Thus, dynamic similarity for the Taylor-Couette flow depends only on the width of the gap between cylinders, the intrinsic properties of the fluid (i.e. viscosity), and the rotation rate (dissipative mechanism) (Landau and Lifshitz 1987, p. 102). We expect this to be a valid expression for the Reynolds number because it completely describes the geometry (length scale) of the system, the velocity scale, and the intrinsic properties of the fluid. Historically, other expressions for the Taylor-Couette Reynolds number have been used to describe the system, and these are also valid, as long as they follow the from of Eq. 2.18 (Van Hook and Shatz 1997, p. 392). More recent publications have also defined and used a *Taylor number*, but we will continue with the conventional Reynolds number stated in Eq. 2.23 (Tagg 1995).

2.6 Applying the linear theory of hydrodynamic stability

To use the linear theory of hydrodynamic stability, we will begin with the equations of motion developed in Section 2.2 and add in a small disturbance, which will either grow or decay over time. The "linear" aspect of the theory means that any number of disturbances may be considered, and each can be analyzed as a separate Fourier component. We will introduce small perturbations in both the velocity field and pressure field as follows:

$$\Delta \boldsymbol{u} = \boldsymbol{u}(r) \exp[i(m\phi + kz) + \sigma t] \tag{2.24}$$

$$\Delta \boldsymbol{p} = \boldsymbol{p}(r) \exp[i(m\phi + kz) + \sigma t], \tag{2.25}$$

where $m,k,$ and σ are all coefficients (Tritton 1988, p. 262). Because $\phi = 0$ and $\phi = 2\pi$ are identical situations, m must be an integer, but the wavenumber k can take any value. Using the simplest case and considering the perturbation to be axisymmetric implies $m =$

0. The time coefficient σ is negative for low Re values and positive above a critical Re value. A negative σ means that the perturbation will tend to decay, while a positive σ means the perturbation will amplify and cause a phase transition (Tritton 1988, p. 262). A lengthy proof by Chandrasekhar has shown that σ is always real, which means that a perturbation will grow or decay continually (Chandrasekhar 1961, p. 43). Thus, the flow will always begin in a laminar form but it will develop patterns as soon the critical Re value is surpassed. For a Taylor-Couette apparatus with a small gap, we merely quote the critical Reynolds number

$$\mathrm{Re}_{cr} = 41.18\left(\frac{a_1}{a_2 - a_1}\right)^{1/2} \tag{2.26}$$

(Chandrasekhar 1961, p. 145). Thus, the Reynolds number acts as a dynamic indicator for studies of the Taylor-Couette flow. It is perhaps counter intuitive, but proven in numerous experiments, that Re_{cr} depends only on the geometry of the system. The theory does not indicate what patterns will form, only where they emerge (where the phase transition occurs), but for this purpose the theory has been proven highly accurate over the last forty years. Small disturbances in the system can amplify spontaneously once the critical Reynolds number has been reached, and this will produce the patterns of the Taylor-Couette flow.

Chapter III

Taylor-Couette flow: experimentation and measurement

3.1 Initial apparatus

For an initial, crude investigation of the Taylor-Couette flow, I constructed an apparatus based on the recommendations of Van Hook and Shatz as published in *The Physics Teacher* (1997, p. 391). The outer cylinder was a standard glass graduated cylinder with radius $a_2 = 2.30 \pm 0.05$ cm, and the inner cylinder was a section of copper tubing with radius $a_1 = 1.60 \pm 0.05$ cm. Using Eq. 2.26, the critical Reynolds number of this system was $Re_{cr} = 62.3$. The inner cylinder was attached to a small DC motor using a plastic shaft adapter. I slid rubber o-rings around the top and bottom of the inner cylinder to keep it aligned in the center of the outer cylinder. The outer cylinder and the motor were held in place using a simple ring stand and two clamps (see Fig 3.1).

Using this apparatus, I observed the transition from laminar flow to Taylor vortices in two different solutions. The first solution used was *rheoscopic fluid*, consisting of distilled water and silica particles (for flow visualization). (Rheoscopic fluid was purchased from Arbor Scientific, Inc.). The second solution was a 50/50 mixture, by volume, of glycerol and distilled water, to which I added a small amount of aluminum powder (particle size ~20 μm) for flow visualization. (Glycerol and aluminum powder were purchased from Sigma-Aldrich Chemical Co.). As expected, due to its much higher viscosity, the water-glycerol solution required a far greater angular speed than the rheoscopic fluid to produce Taylor vortices. Due to the crude nature of the apparatus, I did not take any precise measurements of the angular speed or the viscosity of either solution. After determining that a simple Taylor-Couette apparatus would produce the predicted patterns, I began to construct a larger and far more precise apparatus.

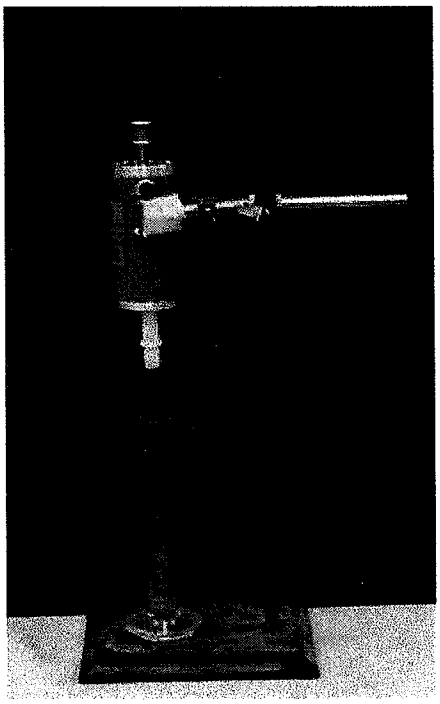

FIG. 3.1. Initial Taylor-Couette apparatus. Section of copper pipe in a 50 ml graduated cylinder that is driven by a DC motor.

3.2 Final apparatus

To investigate the relationships of geometry, viscosity, and angular speed given by Eq. 2.23 and Eq. 2.26, a precise apparatus (see Fig. 3.2) was constructed and four fluids of different viscosities were used. The final apparatus consisted of a polycarbonate outer cylinder (inner radius $a_2 = 5.27 \pm 0.05$ cm and length $l = 56$ cm) and two different PVC plastic inner cylinders (outer radius $a_1 = 4.44 \pm 0.05$ cm, and outer radius $a_1' = 4.22 \pm 0.05$ cm). One of these inner cylinders was solid (negatively buoyant), and the other was partially filled with lead shot to counter-act the buoyancy of the hollow center. The diameters of these cylinders were measured with digital calipers and were determined to be uniform in radius to within the precision of the measurement ($\pm$ 0.05 cm). The motor mount was designed to be removed easily so that the inner cylinders could be exchanged and two different theoretical values of Re_{cr} could be studied with a single apparatus.

Both inner cylinders were fitted with ¼ inch diameter stainless steel shafts. Once an inner cylinder is in place, the shaft fits into bearings constructed of Teflon impregnated plastic located in the base and the polycarbonate cap of the outer cylinder. The shaft enters a shaft adapter 1.5 cm above the upper bearing and the removable polycarbonate cap for the outer cylinder; this adapter is driven by the motor mounted above. The shaft is held in place by a thumb screw (tightened against the flat section of the shaft), and this must be loosened to remove the polycarbonate motor mount and switch cylinders. This is shown in Fig. 3.3. To ensure a precise alignment of the shaft adapter and shaft each time the inner cylinder was switched, the current drawn by the motor was monitored. Because motor drag can be approximately measured by current usage, the cap and motor mount were adjusted in small increments until the motor drew a steady current (and thus a steady drag) at any given rotation rate.

Finding an appropriate DC motor to power the final apparatus was difficult because relatively low cost motors do not run steadily (or at all, in some cases) at the slow speeds ($\Omega = 0.5$ rad/s to 3.5 rad/s) necessary to study the onset of Taylor vortices in the fluids used in this thesis. Attempts were made to control a DC motor by monitoring the signal from an optical encoder (mounted on the motor) and using a lock-in amplifier / operational amplifier system to adjust the motor to follow a function generator. These

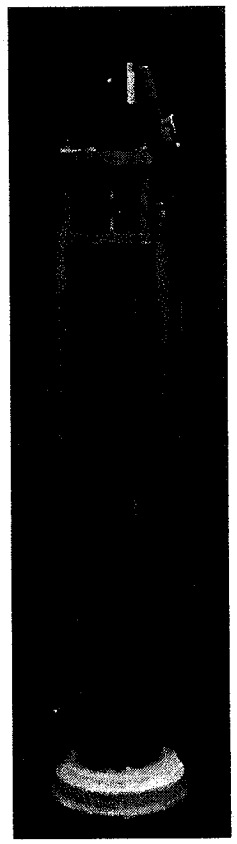

FIG. 3.2. Final Taylor-Couette apparatus (empty).

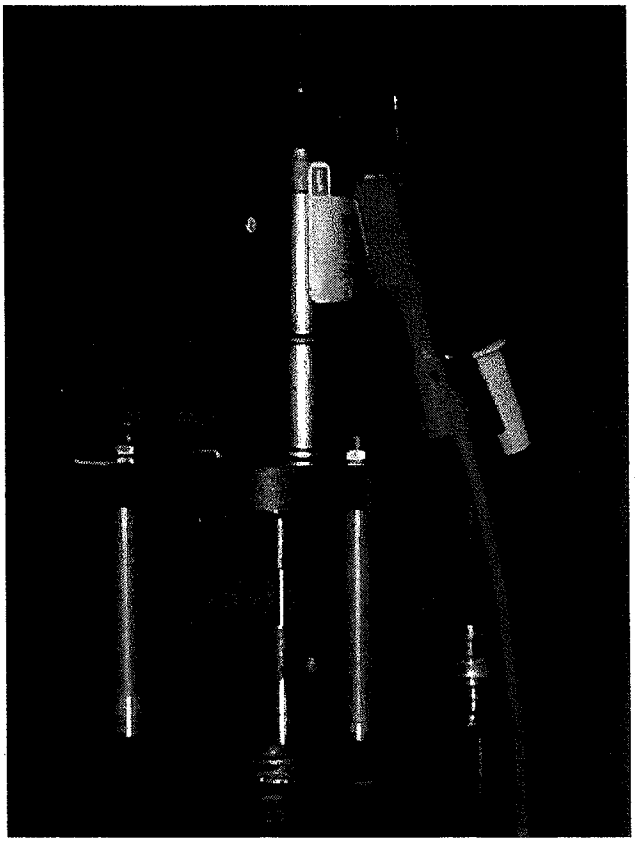

FIG. 3.3. Motor mount and drive shaft adapter of the final Taylor-Couette apparatus.

attempts were unsuccessful. The problem was solved by using a geared down motor (a Pittman #GM9413F277 24V DC motor with a 65.5:1 gear ratio, purchased from C & H Sales, Inc.). The motor was powered by a Hewlett Packard DC power supply (Harrison 6285A) and controlled by limiting the voltage. Two of these motors were purchased and fitted with optical encoders (Hewlett Packard, HEDS-5500 A06), which provide 500 pulses per revolution of the motor. In case of a breakdown, the second motor can be installed by removing the shaft adapter from the motor shaft (using a small hex wrench) and removing the two Phillips head bolts from the upper polycarbonate disk, as shown in Fig. 3.3.

3.3 Measuring viscosity

To produce four fluids with different viscosities, four different solutions of glycerol and rheoscopic fluid were prepared. The viscosities of these solutions were measured using a Gilmont falling ball viscometer (GV-2200). This method of viscosity measurement was first developed by Stokes in 1845 (Sears and Zemansky 1960, p. 280). Stokes deduced that the resistive force R on a sphere falling through a viscous fluid could be expressed by

$$R = 6\pi\mu r v, \tag{3.1}$$

where μ is the viscosity, r is the radius of the sphere, and v is the relative velocity of sphere and fluid (Sears and Zemansky 1960, p. 280). The buoyancy force B due to the density ρ of the fluid could be expressed by

$$B = (4/3)\pi r^3 \rho g, \tag{3.2}$$

and the force of gravity mg on a sphere of density ρ_o is simply $(4/3)\pi r^3 \rho_o g$. Newton's second law shows that the sphere will reach a terminal velocity when the force of gravity equals the sum of the buoyancy force B and the resistive force R, as shown by

$$(4/3)\pi r^3 \rho_o g = (4/3)\pi r^3 \rho g + 6\pi\mu r v. \tag{3.3}$$

By manipulating Eq. 3.3 we can see that the viscosity μ is given by

$$\mu = \frac{2}{9}\frac{r^2 g(\rho_o - \rho)}{v} \tag{3.4}$$

The Gilmont viscometer allows the sphere to drop through a distance d =10.0 cm while moving at its terminal velocity. By knowing the radius of the sphere (r = 0.315 cm) and knowing that $v = d/t$, we can use Eq. 3.4 to realize that the viscosity μ in centipoises (cp) can be determined from

$$\mu = 3.30\,(\rho_o - \rho)t, \tag{3.5}$$

where time t is measured in minutes. For the purpose of this thesis, and for the expression for the Reynolds number, Eq. 2.23, the kinematic viscosity $\nu \equiv \mu/\rho$ is a more useful quantity, and it follows from Eq. 3.5 that

$$\nu = \frac{3.30\,(\rho_o - \rho)t}{\rho}. \tag{3.6}$$

The kinematic viscosity was measured for each solution by first measuring the density of three random samples using a 50 ml graduated cylinder and an OHAUS Precision Standard electric balance. Next, sets of five measurements per sample were taken, using the Gilmont viscosimeter and a stopwatch, on another three random samples of the solution. These results are shown in Table 3.1, and the individual data points are given in appendix A. The results are given in centiStokes, cS, which is a derived unit equal to [cm^2s^{-1} x 10^{-2}]. The motion of the falling sphere through the viscosimeter was extremely sensitive to air bubbles in the fluid. To eliminate this source of error, the sample was left to sit in the viscosimeter tube for 20 minutes before capping, thereby allowing the air bubbles present to rise and escape. Because variations of viscosity with temperature are common, the temperature was monitored throughout the viscosimeter measurements using a Fluke 52 thermocouple. The temperature never left the range from 21.5°C to 22.7°C. Therefore, temperature variations were considered to have a negligible effect upon the viscosity measurements.

The uncertainties for these values were calculated using the standard method of propagating uncertainty in a physical measurement (Young 1962, p. 98). In general, we can determine the uncertainty σ_Q in a result $Q(a,b,c)$ by using the measurement uncertainties σ_a, σ_b, σ_c, and the relation

TABLE 3.1. Properties of experimental solutions.

Solution	Solution #	Density ρ (g/ml)	Kinematic viscosity ν (cS)
40:60, glycerol:water by mass	1	1.080 ± 0.006	3.35 ± 0.08
50:50, glycerol:water by mass	2	1.107 ± 0.006	5.26 ± 0.15
50:50, glycerol:water by volume	3	1.123 ± 0.006	8.65 ± 0.21
65:35, glycerol:water by mass	4	1.154 ± 0.006	12.27 ± 0.22

$$\sigma_Q^2 = \left(\frac{\partial Q}{\partial a}\right)^2 \sigma_a^2 + \left(\frac{\partial Q}{\partial b}\right)^2 \sigma_b^2 + \left(\frac{\partial Q}{\partial c}\right)^2 \sigma_c^2 . \tag{3.7}$$

By applying this method to the density $\rho = m/V$, we can express the uncertainty in ρ by

$$\sigma_\rho = \sqrt{\frac{\sigma_m^2}{V} + \left(\frac{-m}{V^2}\right)^2 \sigma_V^2} = \rho \sqrt{\frac{\sigma_m^2}{m^2} + \frac{\sigma_V^2}{V^2}} . \tag{3.8}$$

Thus, the density values in Table 3.1 include an uncertainty propagated from the ± 0.01 g uncertainty in mass measurement and the ± 0.25 ml uncertainty in volume measurement. These uncertainties are similar and often greater than the standard deviations of an actual set of density measurements, and thus these propagated uncertainties seem appropriate.

The uncertainty in kinematic viscosity measurements is due the ± 0.015 minute (~ 1 second) uncertainty in the drop time t and the uncertainty of each density measurement, and it is given by

$$\sigma_\nu = \sqrt{\left(\frac{3.3(\rho_o - \rho)}{\rho}\right)^2 \sigma_t^2 + \left(\frac{3.3\rho_0 t}{\rho^2}\right)^2 \sigma_\rho^2} . \tag{3.9}$$

These propagated uncertainties were all smaller than the standard deviation of each data set. Thus, the standard deviations were more conservative measures of uncertainty for these measurements, and these values were used to quote the uncertainties in kinematic viscosity found in Table 3.1. The full data sets are given in Appendix A.

3.4 Measuring angular speed

Each of the four fluids was tested using both inner cylinder sizes. The voltage supplied to the motor was slowly increased until the critical angular speed Ω_{cr} required for Taylor vortices was reached. This critical speed was measured by the optical encoder mounted on the motor, which was powered by a Hewlett Packard DC power supply (#6281A) set at 5.0 V. The Channel A output of the encoder sends 500 pulses per motor shaft revolution to a LeCroy digital oscilloscope. The oscilloscope was set to measure the frequency of these pulses. Dividing this frequency by (500 x 65.5) and multiplying by 2π gives the angular frequency Ω of the drive shaft (and inner cylinder). Because the

frequency varied slightly, twenty measurements of the frequency were recorded per trial (using the oscilloscope 'run/stop' button). Five trials were conducted for each fluid with the small inner cylinder, and five trials were conducted for each fluid with the large inner cylinder. Thus, a total of 100 measurements of the critical speed Ω_{cr} were taken for each cylinder-fluid setup. The results are shown in Table 3.2, with the standard deviation of each data set used as the uncertainty in measurement.

Although the motor speed was not stabilized an electronic feedback loop, the percent standard deviation (used here as the fractional uncertainty) in angular speeds was normally around one percent. Constant rotation would have been ideal, but this motor system was deemed adequate because the fractional uncertainties in the other experimental measurements were no more precise than one percent. The full data sets and the standard deviations are recorded in Appendix A, and Appendix B contains pictures of each cylinder-fluid setup. These measurements will be used in Chapter IV to verify the application of the linear theory of hydrodynamic stability to the onset of Taylor vortices.

Chapter IV

Taylor-Couette flow: analysis

4.1 Experimental determination of Re_{cr}

The 800 measurements of Ω_{cr} (see Appendix A) taken in order to produce the results reported in Section 3.4 show clearly that there is a precise critical point for a given geometry and fluid at which laminar flow is no longer stable and Taylor vortices form. Examples of laminar flow and Taylor vortices seen experimentally are shown in Fig. 4.1; the Taylor vortices of each cylinder-fluid system are shown in photographs in Appendix B. As stated in Section 2.5, we can quantify the dynamics of the system using the Reynolds number as given in Eq. 2.23. Thus, the critical Reynolds number Re_{cr} for a given experiment will be

$$Re_{cr} = \frac{\Omega_{cr} a_1 (a_2 - a_1)}{\nu}. \tag{4.1}$$

It is important to note that the kinematic viscosity ν in this equation must be in units of cm^2/s (converted using 10^{-2} cm^2/s = 1 cS) because the radius measurements are in centimeters. These Re_{cr} values are shown below in Table 4.1, and depicted graphically in Fig. 4.2. Theoretically the linear best-fit lines should be exactly horizontal (universal Re_{cr} for each geometry), and the experimental data is not far from this prediction. The fractional standard deviation of Re_{cr} was 2.8% for large a_1 and 3.8% for small a_1', and thus a nearly universal Re_{cr} was found for each of the two geometries.

Again, using the standard method for propagation of uncertainty shown in Eq. 3.7, the uncertainty for each Re_{cr} was determined from the uncertainty in each measured quantity as

follows

$$\sigma_{Re} = \sqrt{\left(\frac{a_1(a_2 - a_1)}{\nu}\right)^2 \sigma_\Omega^2 + \left(\frac{\Omega(a_2 - 2a_1)}{\nu}\right)^2 \sigma_{a_1}^2 + \left(\frac{\Omega a_1}{\nu}\right)^2 \sigma_{a_2}^2 + \left(\frac{\Omega a_1 (a_2 - a_1)}{\nu^2}\right)^2 \sigma_\nu^2}. \tag{4.2}$$

TABLE 3.2. Critical angular frequencies Ω_{cr} for each solution and geometry.

Solution #	Large inner cylinder $a_1 = 4.44$ cm angular frequency Ω_{cr} (rad/s)	Small inner cylinder $a_1' = 4.25$ cm angular frequency Ω_{cr} (rad/s)
1	0.983 ± 0.027	0.756 ± 0.037
2	1.447 ± 0.015	1.087 ± 0.008
3	2.497 ± 0.015	1.860 ± 0.008
4	3.436 ± 0.012	2.570 ± 0.015

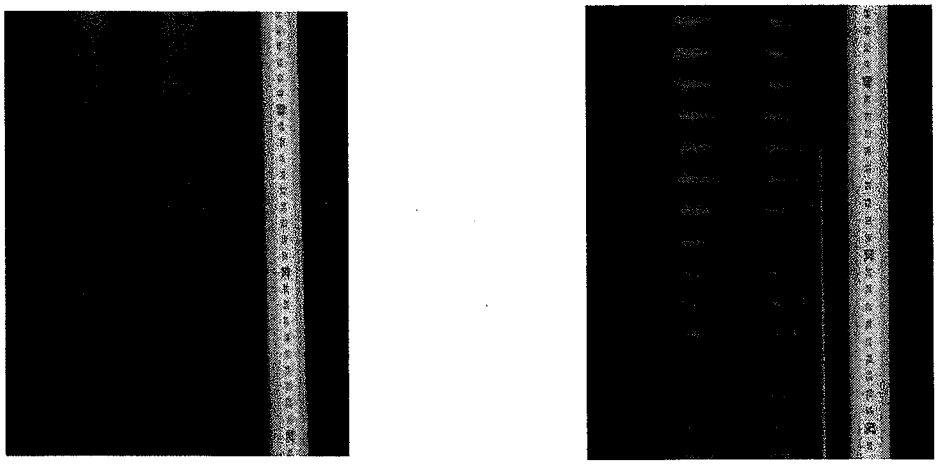

(a) (b)

FIG. 4.1. Experimental Taylor-Couette results using Solution #2;
(a) laminar flow and (b) Taylor vortices.

TABLE 4.1. Experimentally determined critical Reynolds numbers.

Solution #	Large inner cylinder $a_1 = 4.44$ cm critical Reynolds number Re_{cr}	Small inner cylinder $a_1' = 4.25$ cm critical Reynolds number Re_{cr}
1	103.1 ± 0.2	79.3 ± 0.1
2	96.9 ± 0.1	72.8 ± 0.1
3	101.6 ± 0.1	75.7 ± 0.1
4	98.6 ± 0.1	73.8 ± 0.1
fractional standard deviation	2.8 %	3.8 %

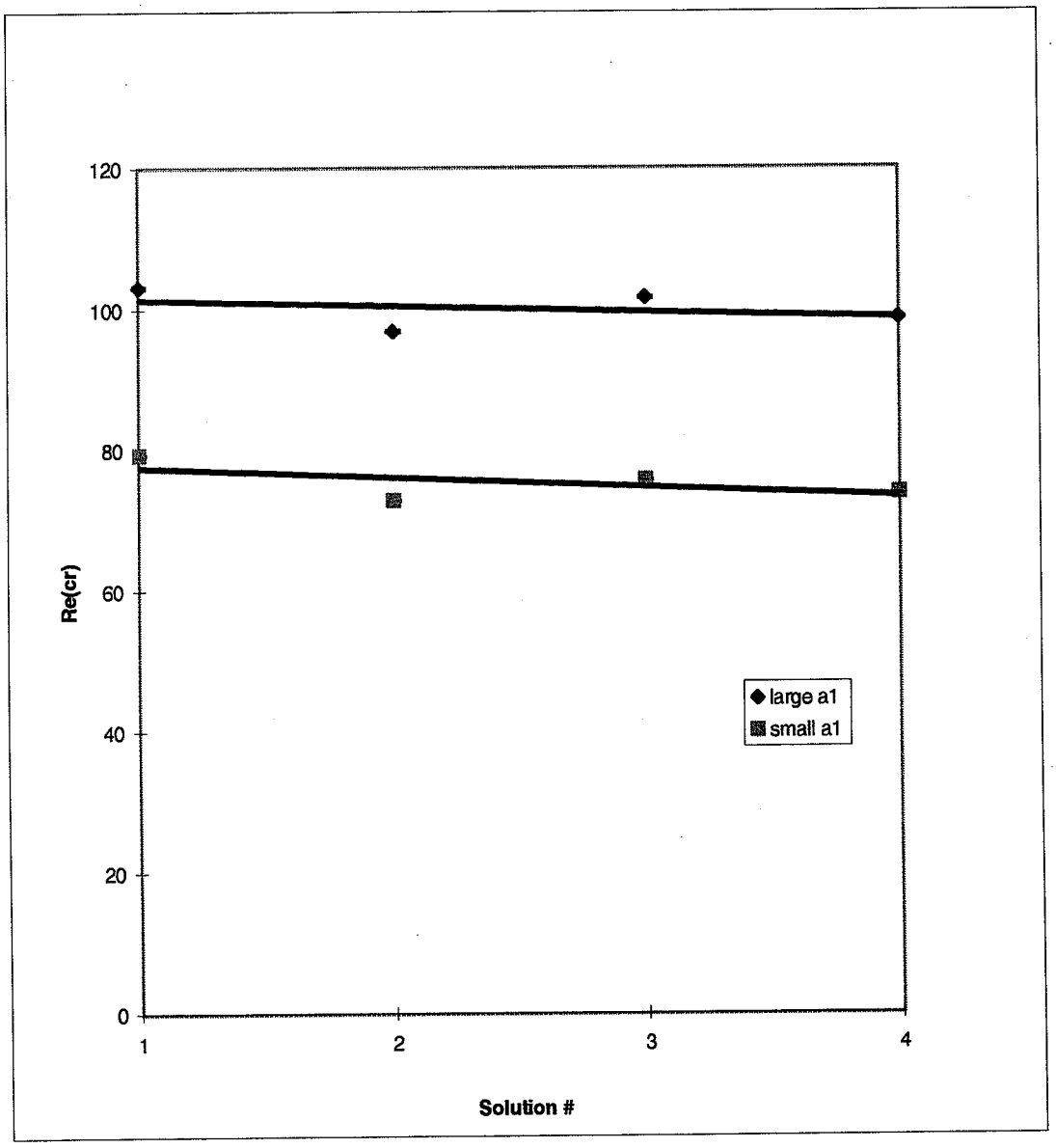

FIG. 4.2. Experimentally determined critical Re for two geometries (two inner cylinder sizes), using four solutions. Solid lines are linear best-fits of the data for each inner cylinder; theoretically these lines should be horizontal.

To be more exact, we expect this critical value of the Reynolds number to be universal for a given geometry. If the Reynolds number is constant, the angular speed Ω_{cr} should be exactly inversely proportional to the viscosity ν for the each inner cylinder. This relation is shown by the two nearly straight lines (one for each a_1 value) in Fig. 4.3.

4.2 Theoretical Re_{cr}

Now that we have examined the nature of the critical point for instability in the Taylor-Couette system, let us investigate Chandrasekhar's prediction of the critical Reynolds number for the case of a small gap, $(a_2 - a_1) << a_1$, as given by Eq. 2.26

$$\mathrm{Re} = 41.18\left(\frac{a_1}{a_2 - a_1}\right)^{1/2}. \tag{4.3}$$

In this exploration, it quickly becomes apparent that the small inner cylinder (the larger gap) is somewhat outside the range of Chandrasekhar's approximation. As described in Section 3.2, the inner radius of the outer cylinder is $a_2 = 5.27 \pm 0.05$ cm and the two inner cylinders have radii of $a_1 = 4.44 \pm 0.05$ cm and $a_1' = 4.25 \pm 0.05$ cm. The system with the larger inner cylinder has a ratio $(a_2 - a_1)/a_1$ of 0.19, while the system with the smaller inner cylinder has a ratio $(a_2 - a_1)/a_1$ of 0.24. As will be shown later, the system that is closer to the $(a_2 - a_1) << a_1$ requirement produced results more consistent with Eq. 4.3.

Once more we apply the standard method for propagation of uncertainty, Eq. 3.7, and we find that the uncertainty σ_{Re} in the Re_{cr} prediction results from the uncertainties in measuring a_1 and a_2 through

$$\sigma_{\mathrm{Re}} = \sqrt{\frac{41.18^2}{4}\left(\frac{a_2^2\sigma_{a_1}^2}{a_1(a_2 - a_2)^3} + \frac{a_1\sigma_{a_2}^2}{(a_2 - a_1)^3}\right)}. \tag{4.4}$$

Application of Eq. 4.4 shows us that a small error in the measurement of a cylinder's radius or a slight error in axial alignment will have a dramatic effect upon the theoretical Re_{cr} value; the inability to verify the uniformity of each cylinder's radius throughout its length is unquestionably the largest source of error in this thesis. This is an ideal example

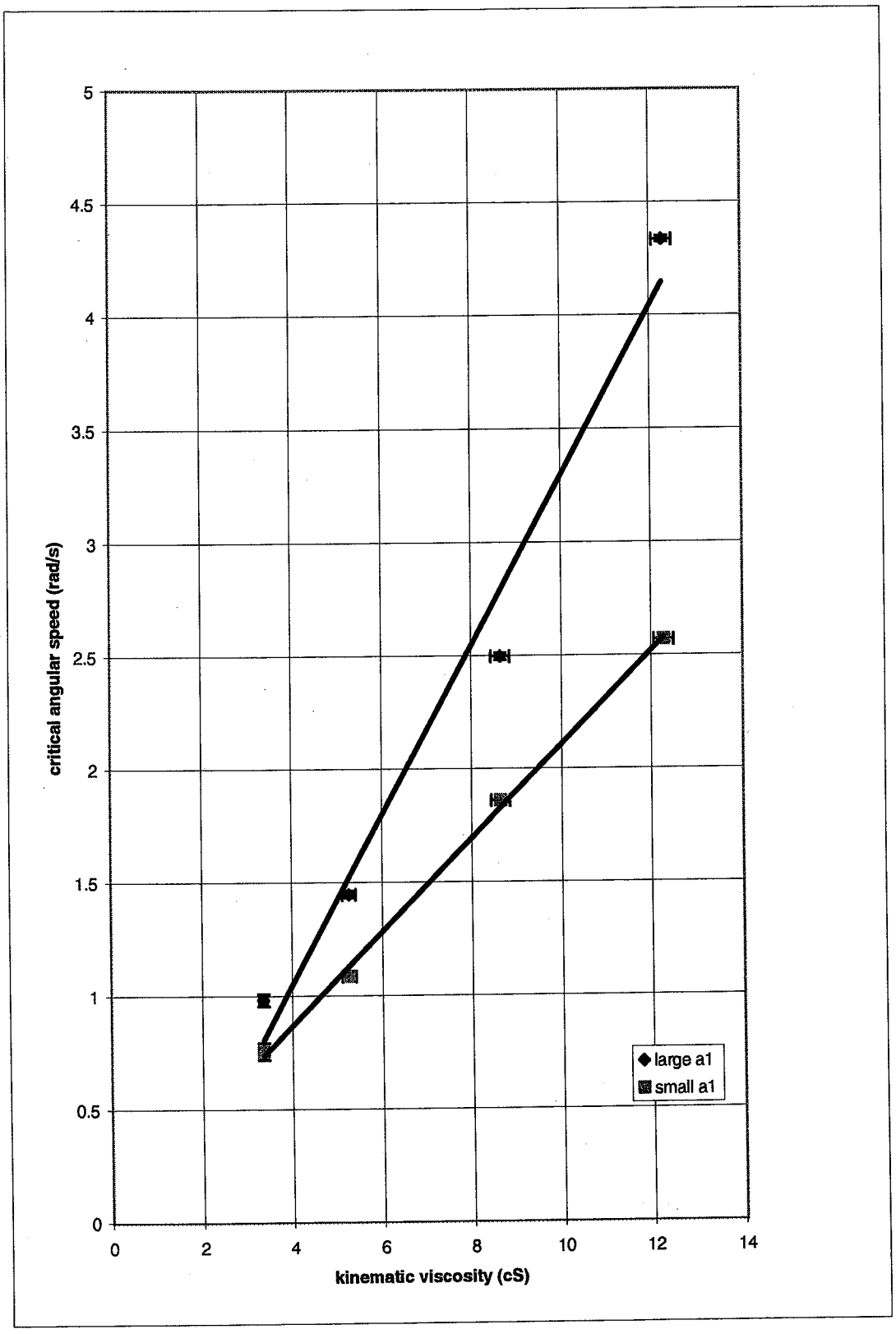

FIG. 4.3. Dependence of critical angular speed on viscosity for two fixed geometries; solid lines are linear best-fits of the data.

of a system with extreme sensitivity to geometric conditions, and it is a common theme in complexity analysis. Using Eqs. 4.3 and 4.4, we obtain the following theoretical values: $Re_{cr}(a_1 = 4.44\text{ cm}) = 95.2 \pm 4.5$ and $Re_{cr}(a_1 = 4.25\text{ cm}) = 84.1 \pm 3.3$. Figure 4.4 shows these theoretical Re_{cr} values along with the experimentally obtained values. The experimental data points for the large inner cylinder (smaller gap) generally fall within the uncertainty of the theoretical values, but the experimental points of the small inner cylinder (larger gap) are clearly below the theoretical Re_{cr} obtain from Eq. 4.3. Thus, the data suggests that Chandrasekhar's small gap approximation is not accurate for a system with a geometric ratio $(a_2 - a_1)/a_1 \geq 0.24$.

4.3 Pattern selection

Of particular interest in this system is the patterns themselves. As discussed below, the patterns are actually very similar in size to the gap between the cylinders, and this is perhaps another example of sensitivity to spatial conditions. This result seems intuitive, but when considered analytically it is quite amazing that the system's emergent behavior is so well predicted by consideration of the boundary conditions.

Linear stability theory predicts that there will be a *critical wavelength* (maximum voritice size measured in the z direction) to the emergent Taylor vortices, which is dependent upon the geometry of the system. However, this theory does not require that the critical wavelength is always chosen by the system (Koschmieder 1993, p. 242). Linear stability theory simply predicts the critical point when the flow becomes unstable, and this instability results in pattern formation. Thus, just as we will see later in convection, the patterns are non-unique. As experimentally verified by Burkhalter and Koschmieder (1974), the vortices may form in different sizes depending on how slowly or quickly Re_{cr} is approached. According to theory, we do expect the pattern wavelength λ to be uniform throughout the system at any given time, and we expect λ to be the same when Re_{cr} is approached in the same way.

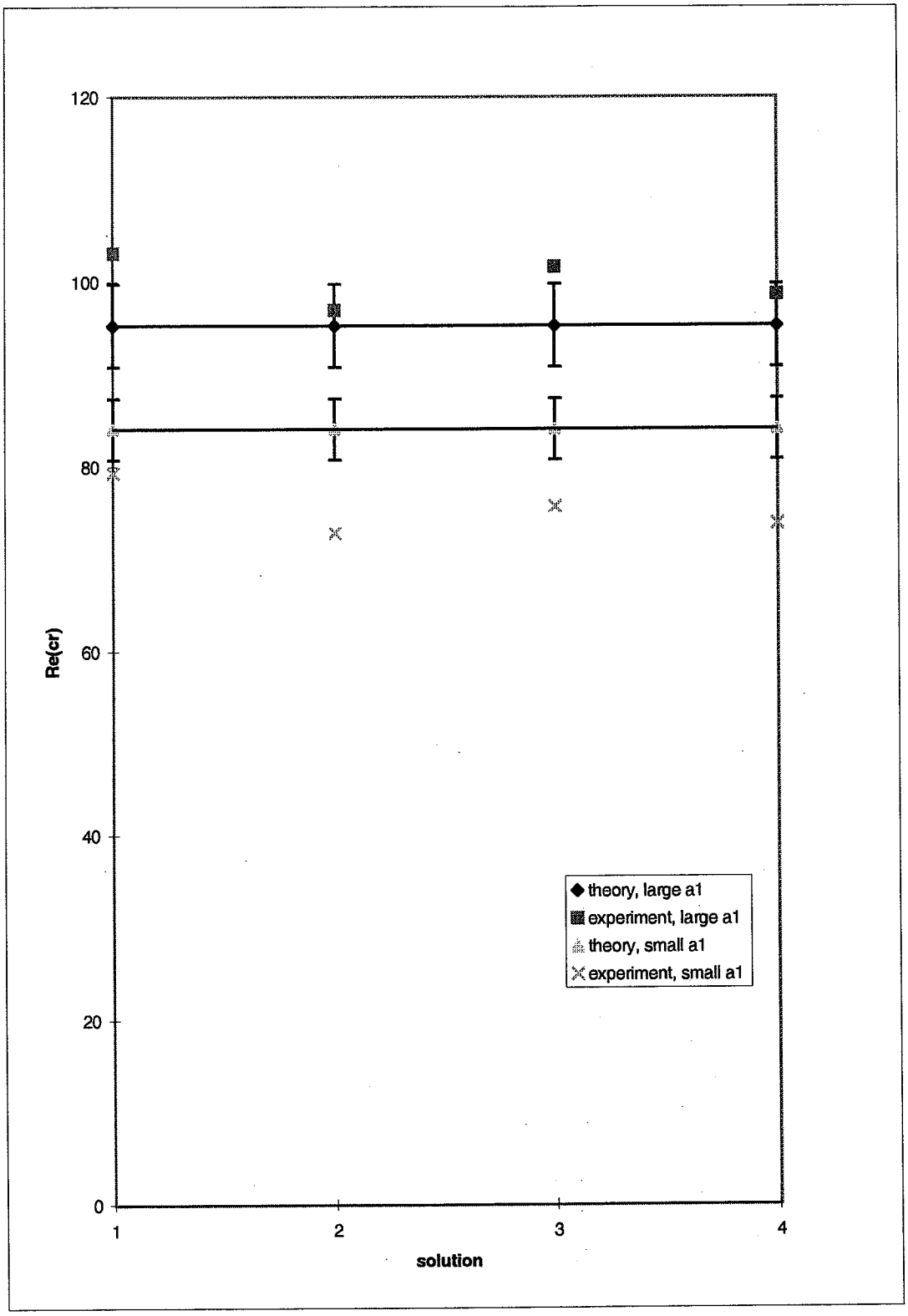

FIG. 4.4. Experimentally and theoretically determined critical Re. Horizontal lines represent the theoretical 'small gap' aproximation, Eq. 4.3, and error bars correspond to uncertainty in theoretical values.

The Taylor vortices were measured at Re_{cr} during each experimental run, and the results were exceptionally consistent, as shown in Table 4.2. The critical Reynolds number was approached slowly from $\Omega = 0$ during each run, and the pattern wavelength λ was consistently 0.85 ± 0.05 cm for the system with large a_1 and 1.05 ± 0.05 cm for the system with small a_1'. It is interesting to note that the ratio of the gap distance between cylinders and the wavelength λ is the same (within 1%) for both inner cylinder sizes. This further confirms the notion that pattern size is a function of geometry alone and arises from the boundary conditions of the system.

4.4 Beyond Re_{cr}

After studying the initial bifurcation into unstable flow at Re_{cr}, each system was driven further in the supercritical regime. This study was not nearly as thorough or meticulous as the examination of Re_{cr}, yet these limited observations are still useful for understanding the emergence of complexity in the Taylor-Couette flow. A comprehensive discussion of the supercritical regime in can be found in Koschmieder (1993). When driven beyond Re_{cr}, the eight systems all made a transition from straight Taylor vortices to wavy Taylor vortices (see Fig. 4.5) once a Reynolds number beyond at least 1.25 Re_{cr} had been reached. This emergence of patterns that are no longer axis-symmetric is intrinsic to our application of linear stability theory, and is the amplification of perturbations that are no longer axisymmetric. (Meaning that $m \neq 0$ in the perturbation equations Eqs. 2.24 and 2.25). The Reynolds numbers for the emergence of wavy vortices are given in Table 4.3.

It is interesting to note that the larger gap (small a_1') consistently had to be driven much farther above Re_{cr} to produce wavy Taylor vortices, as shown in Fig. 4.6a. The small a_1 system required lower Re values than the large a_1 system to produce axis-symmetric vortices, and yet the small a_1' system required much higher Re values than the large a_1 to produce wavy vortices. Figure 4.6b shows that viscosity, and not geometry alone, is a factor in the emergence of these wavy vortices. Both geometric systems

TABLE 4.2. Pattern wavelength, λ, and gap-wavelength ratio.

Solution #	Large inner cylinder a_1= 4.44 cm pattern wavelength λ (cm)	Small inner cylinder a_1'= 4.25 cm pattern wavelength λ (cm)
1	0.85 ± 0.05	1.05 ± 0.05
2	0.85 ± 0.05	1.05 ± 0.05
3	0.85 ± 0.05	1.05 ± 0.05
4	0.85 ± 0.05	1.05 ± 0.05
Ratio $\frac{(a_2 - a_1)}{\lambda}$	0.976	0.971

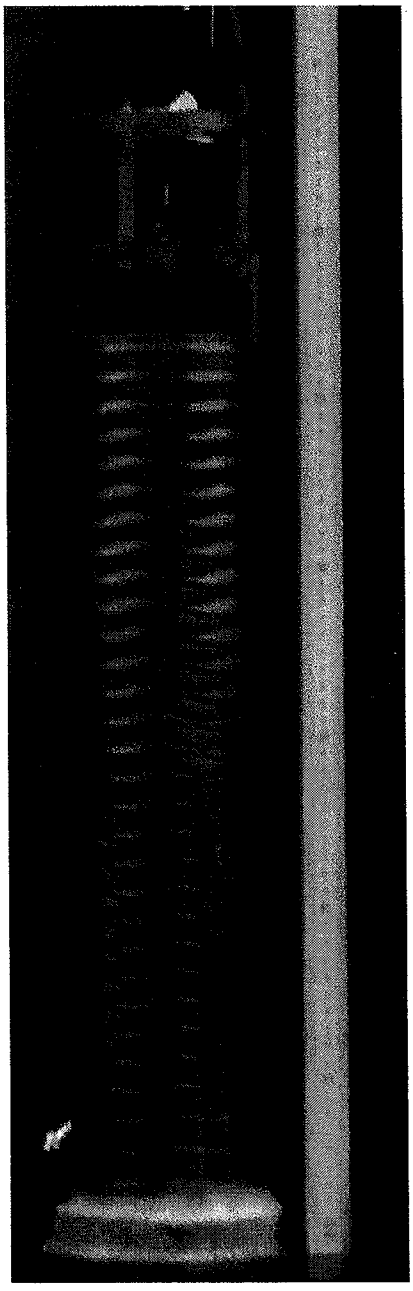

(a)

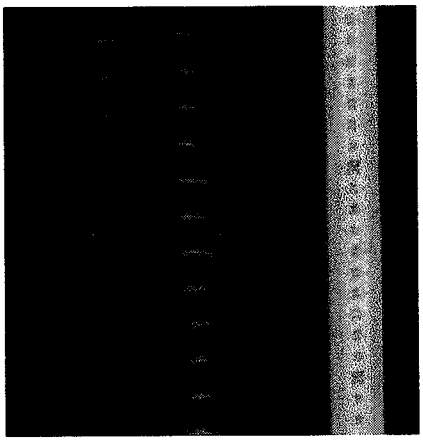

(b)

FIG. 4.5. Wavy Taylor vortices using Solution # 2; (a) entire apparatus and (b) close-up.

TABLE 4.3. Supercritical flow: observed Reynolds number for emergence of 'wavy' Taylor vortices, and the ratio of Re_{wavy} to Re_{cr}.

Solution #	Large inner cylinder a_1= 4.44 cm		Small inner cylinder a_1'= 4.25 cm	
	Re_{wavy}	Re_{wavy}/Re_{cr}	Re_{wavy}	Re_{wavy}/Re_{cr}
1	194	1.88	379	4.79
2	141	1.46	301	4.14
3	139	1.37	286	3.78
4	150	1.52	173	2.35

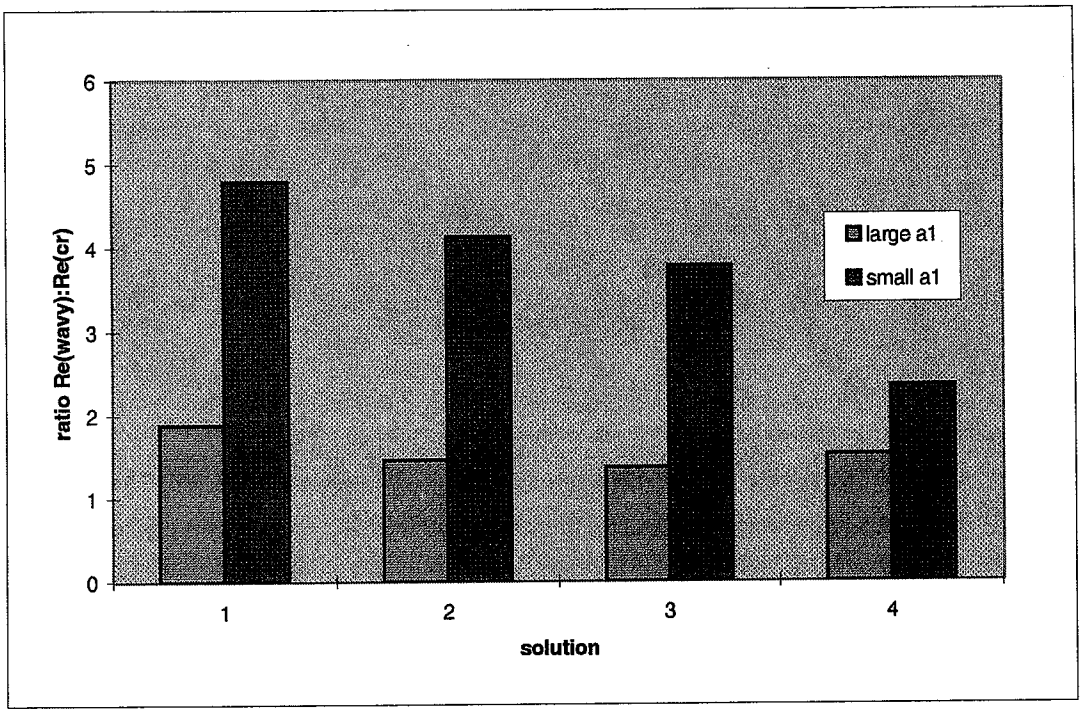

(a)

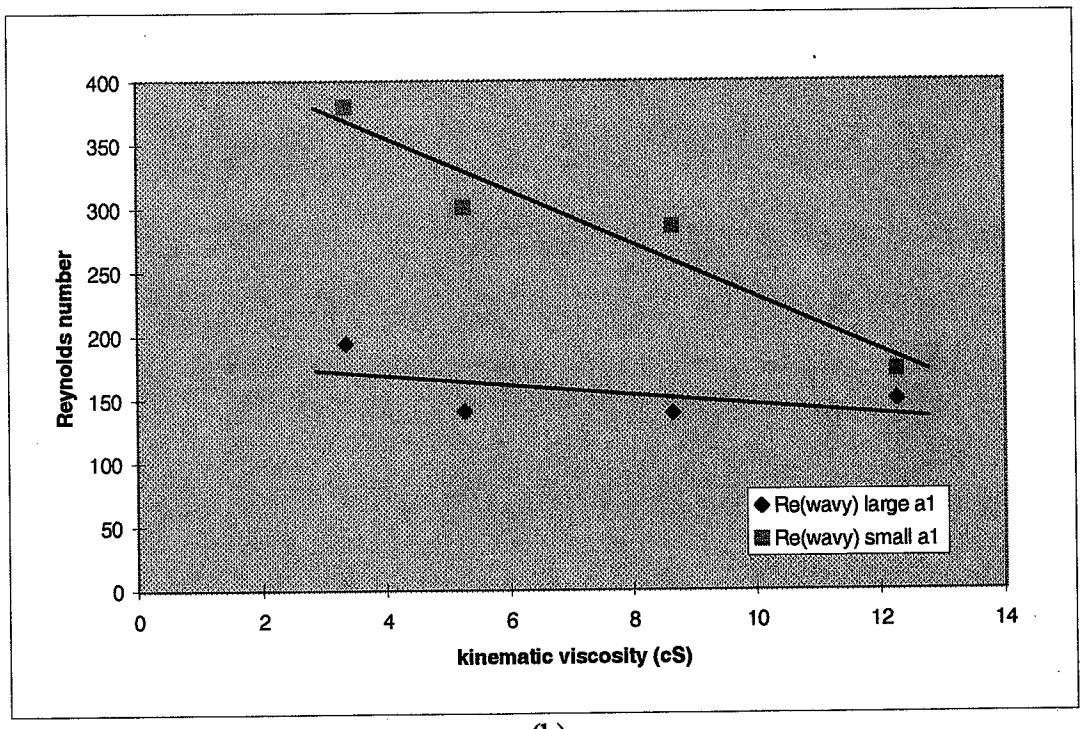

(b)

FIG. 4.6. Reynolds numbers for the emergence of wavy Taylor vortices; (a) the observed ratio of the critical Re to the wavy Re in each experimental case, and (b) the viscosity dependence of wavy Re; solid lines represent linear best-fits of the data for the two geometries.

produce wavy vortices at lower Reynolds numbers with fluids of greater viscosity, although the effect is far greater in the large gap system.

When the system was driven further into the supercritical regime, turbulent flow occured. At first this flow was contained with the Taylor vortices (an example of chaos within a structured system), which eventually became axisymmetric again (see Fig. 4.7). When driven to exceptionally high Reynolds numbers (on the order of 1000 Re_{cr}), the flow became fully turbulent. A second motor (Pittman #14203d244-R2, 38.2V DC) was required to reach such high angular speeds. Unfortunately, the apparatus shakes violently at these speeds and needs to be mechanically stabilized before more research is done within the turbulent regime.

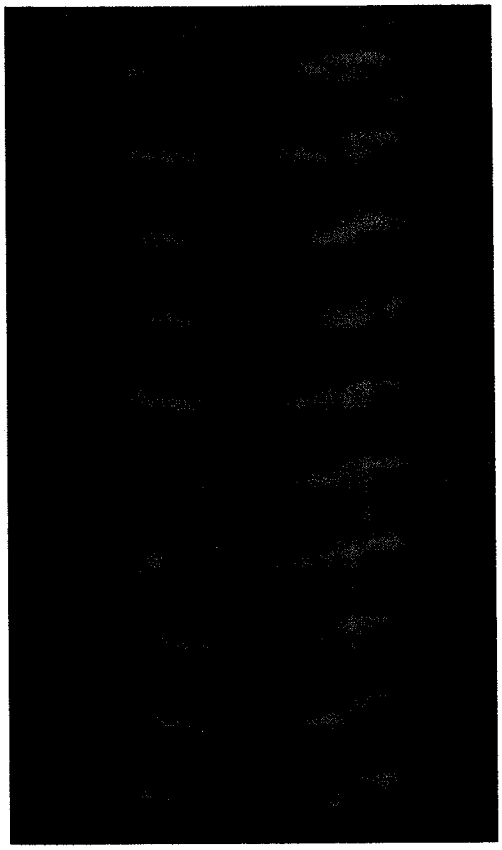

FIG. 4.7. Turbulent Taylor vortices using Solution #2.

Chapter V

Benard convection: history and theory

5.1 History

In 1897, Henri Benard undertook the first scientific study of convection in a thin layer of fluid heated from below. Benard produced hexagonal convection patterns in spermaceti (whale oil) by heating the underside of the fluid with brass and cast iron plates held over boiling water and cooling the topside with air. Benard was conscious of the asymmetry in boundary conditions that resulted from this free surface (topside open to air and therefore not uniform cooling), yet he felt the free surface was necessary to view the convective patterns. The depth of the fluid was on the order of 1 mm, and the temperature difference across the fluid was around 80°C (Koschmieder 1993, p. 5). Although many of the images in his work show patterns that are closer to diverse polygons, Benard was convinced that uniform hexagonal convection patterns were possible. Benard was also convinced that the convection patterns being formed were due to buoyancy (hot fluid rising, cold fluid falling), and he published his results as his doctoral thesis in 1900 (Tritton 1988, p. 42).

In 1916 J.W.S. Rayleigh presented a framework for understanding the patterns Benard observed in terms of hydrodynamic stability (similar to the discussion of stability in the Taylor-Couette flow, Section 2.6). This work is the foundation of our modern understanding of Benard convection. Because of the significance of Rayleigh's work and his insight into the control parameter for the convective system, buoyancy driven convection is now commonly know as Rayleigh-Benard convection. However, it was discovered by J.R.A. Pearson in 1958 that the convection seen by Benard was actually driven by surface tension forces and not by buoyancy forces (Koschmieder 1993, p. 37). To follow convention, fairly attribute credit, and avoid confusion, we will refer to the buoyancy driven case as Rayleigh-Benard convection and to the surface tension case as Marangoni-Benard convection (for Marangoni's work in developing the control

parameter for the surface tension case). Since Pearson's discovery and Chandrasekhar's extensive work in hydrodynamic stability theory during the 1960s, a large volume of theoretical and experimental work has been done on both forms of convection, yet the general application of linear stability theory has remained. Although it will be somewhat less in-depth than the discussion of the Taylor-Couette flow, we will now go through a description of the modern understanding of the formation of convection patterns.

5.2 Linear theory of hydrodynamic stability

Just as in the Taylor-Couette flow, linear stability theory can be used to predict and describe the phase transitions in a convective system. When a thin layer of fluid is heated from below, as shown in Fig. 5.1a, the fluid will be at rest when the dissipative forces of viscosity and thermal conductivity are greater than the driving, or destabilizing, force of the temperature difference (Tritton 1988, p. 42). When the system reaches a critical balance point between driving and dissipative forces, the system will become unstable to small disturbances that are *already present in the system.* A small disturbance will amplify and cause the system to undergo a phase transition and enter a state of motion (Tritton 1988, p. 255). This motion is described in Fig. 5.1b. It is important to note that motion does not result due to an absence of equilibrium, but simply because the motionless state is unstable (Tritton 1988, p. 42). There are still solutions to the Navier-Stokes equation in which the fluid could be at rest, but because the state is unstable these solutions do not occur.

5.3 The Boussinesq approximation

Our discussion of convection will only be concerned with externally induced temperature variations. We will not be concerned with flow-induced temperature variations, but restrict our analysis to temperature variations between boundaries (more specifically between a rigid boundary and air, an ambient fluid). Thus, the temperature will be considered a continuous function of position $T = T(\boldsymbol{r})$. In principle, temperature

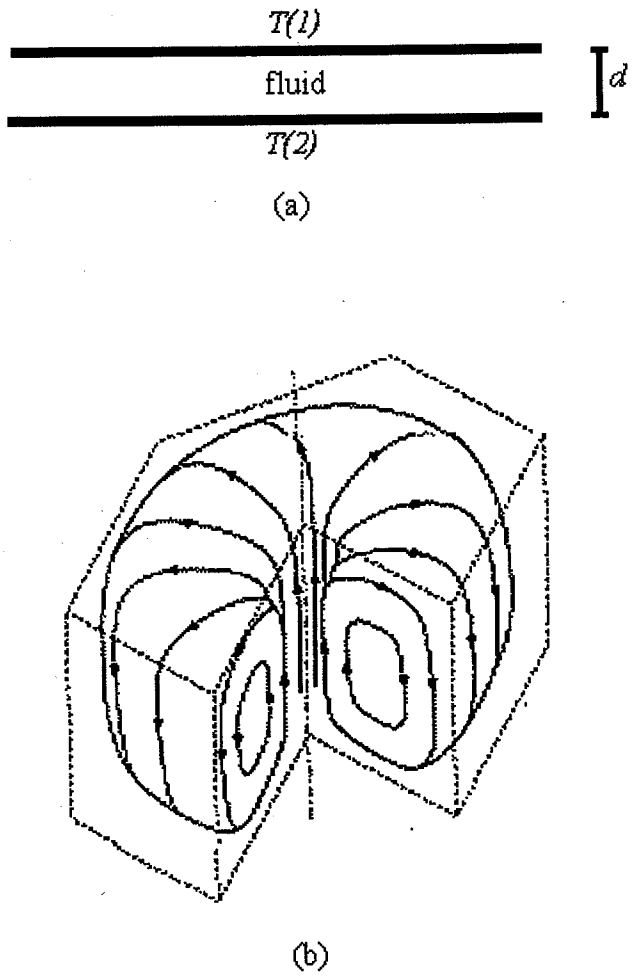

FIG. 5.1. Benard convection (a) boundary conditions and (b) motion within convection cells (Koschmieder 1993, p. 30).

variations will give rise to variations in the properties of the fluid, but including this in our analysis would be extremely complicated and outside the scope of this thesis. Therefore we will make the commonly used *Boussinesq* approximation, which considers all fluid properties (viscosity, thermal conductivity, coefficient of expansion, etc.) except the density to remain constant[1] (Koschmieder 1988, p.14). In fact, the density is considered constant except in regards to the contribution of the gravitational force. Thus the continuity equation Eq. 2.1 again reduces to

$$\nabla \cdot \boldsymbol{u} = 0, \tag{5.1}$$

just as in Taylor-Couette flow (Tritton, 164). Likewise, we introduce a constant density ρ_0 into the Navier-Stokes equation

$$\rho_0 \frac{\mathrm{D}\mathbf{u}}{\mathrm{D}t} = -\nabla p + \mu \nabla^2 \mathbf{u} + \mathbf{F}. \tag{5.2}$$

5.4 Rayleigh-Benard convection

Rayleigh-Benard convection is the result of hot, less dense fluid rising as cold, more dense fluid sinks. Much work has been done to analyze the structure, size, and *planform* (shape) of the resulting convection patterns; however, we will restrict our discussion to understanding when and how these patterns form. In the Navier-Stokes equation, Eq. 5.2, we now include a body force term (instead of setting $\boldsymbol{F} = 0$, as we did in the Taylor-Couette case), and this body force is the gravitational force due to a change in density, as follows

$$\boldsymbol{F} = \rho g \qquad \text{with} \qquad \rho = \rho_o + \Delta\rho \tag{5.3}$$

(Tritton 1988, p. 164). We are able to consider the density ρ to be constant for all other terms of Eq. 5.2, because when $\Delta\rho/\rho_o << 1$ and all accelerations in the flow are small compared to g, the only significant effect of $\Delta\rho$ is in the body force term. We must make another approximation and linearize $\rho(T)$ using the volume coefficient of expansion of the fluid, α, and writing

[1] The full development of the Boussinesq approximation is described in *Stability of Fluid Motions* (Joseph, 1976). The implications have been studied by Spiegel and Veronis (1960), Mihaljan (1962), Perez-Cordon and Velarde (1975), and Gray and Giorgini (1975).

$$\Delta\rho = -\alpha\rho_o\Delta T \tag{5.4}$$

(Tritton 1988, p. 164). The dynamical equation Eq. 5.2 now becomes

$$\frac{D\boldsymbol{u}}{Dt} = -\frac{1}{\rho}(\nabla p) + \nu\nabla^2\boldsymbol{u} - g\alpha\Delta T \tag{5.5}$$

(Tritton 1988, p. 164). Equation 5.5 is the dynamical equation for a buoyancy driven layer of fluid.

We also need an equation for the temperature T. We will assume that the fluid has a constant heat capacity per unit volume, expressed as ρC_p, and we will again use the substantive derivative operator of Eq. 2.5; in this case, to express the change in temperature DT/Dt as we follow a fluid particle (Tritton 1988, p. 165). Thus, we can express the rate of heating per unit volume as $\rho C_p\left(DT/Dt\right)$; this heating is due solely to the transfer of heat from neighboring fluid particles by thermal conduction.[2] We define the conductive heat flux $\boldsymbol{H}$ as

$$\boldsymbol{H} \equiv -k\nabla T, \tag{5.6}$$

where k is the thermal conductivity of the fluid and considered constant (Tritton 1988, p. 165). We then equate the divergence of the conductive heat flux to the rate of heating per unit volume,

$$\rho C_p\left(DT/Dt\right) = -\nabla\cdot\boldsymbol{H}. \tag{5.7}$$

Using Eq. 2.5 and the definition of the substantive derivative operator, we can now arrive at the thermal equation for convection

$$\frac{\partial T}{\partial t} + \boldsymbol{u}\cdot\nabla T = \kappa\nabla^2 T, \tag{5.8}$$

where $\kappa \equiv k/\rho C_p$ is the thermal diffusivity, or thermometric conductivity, of the fluid (Tritton 1988, p. 165).

Now that we have developed the continuity equation, Eq. 5.1, the dynamical equation, Eq. 5.5, and the thermal equation, Eq. 5.8, we can apply these to the case of a horizontal layer of fluid (thickness d) contained between two boundaries of constant

[2] To be truly general, the thermal equation we are building should include a term for internal heat generation, but we will consider it negligible in this analysis.

temperatures T_1 and T_2. The concept of dynamic similarity (Section 2.5) is, of course, completely relevant to this system, but the Reynolds number does not fully describe the system. Thus we must follow convention and introduce the *Rayleigh number* Ra as the control parameter for convection. For the circumstances of Rayleigh-Benard convection, it is given by

$$\mathrm{Ra} = \frac{g\alpha(T_2 - T_1)d^3}{\nu\kappa} \tag{5.9}$$

(Landau and Lifshitz 1987, p. 219). Similar to the Taylor-Couette case, the system becomes unstable to small disturbances once driven beyond a critical value of the control parameter. The theoretical critical Rayleigh value for rigid boundary conditions (T_1 above fluid; T_2 below fluid) is $\mathrm{Ra}_{cr} = 1708$. This result is reached with the same methods as in the Taylor-Couette analysis. We introduce small perturbations in the velocity field, temperature, and pressure of the form

$$\boldsymbol{u} = \boldsymbol{U}(z)\exp[i(k_x x + k_y y) + \sigma t], \tag{5.10a}$$

$$p = p(z)\exp[i(k_x x + k_y y) + \sigma t], \tag{5.10b}$$

$$T = T(z)\exp[i(k_x x + k_y y) + \sigma t], \tag{5.10c}$$

and these perturbations amplify (time coefficient $\sigma > 0$) when the system is above Ra_{cr} (Tritton 1988, p. 362). For values below Ra_{cr} the time coefficient is negative and these disturbances decay quickly. The fluid is at rest until Ra_{cr} is reached, at which point movement occurs due to instability. The most well known and celebrated flow above Ra_{cr} is the emergence of hexagonal convection cells (shown in Fig. 1.2), yet this is only one possible configuration. Long, straight convection rolls are also common experimentally. Linear stability theory simply predicts when the phase transition will occur; no prediction of pattern selection is given without introducing far more complicated and lengthy non-linear analysis. Despite this shortcoming, linear stability theory has been shown experimentally to be very successful for the prediction of the onset of convection.

5.5 Marangoni-Benard Convection

Although perhaps more intuitive and comprehensible, Rayleigh-Benard convection presents difficult problems in practical experimental work, and the surface-tension case (Marangoni-Benard convection) is more readily accessible to experimental investigation. As described later in Chapter 6, these experiments deal with a rigid lower boundary surface of constant temperature and an upper 'free' boundary surface of constant temperature (air, in this case). For this discussion, we will modify the Boussinesq approximation and assume that all fluid properties, including density ρ, are constant, except the surface tension coefficient S. We will now consider a thin fluid layer, in which gravity is neglected and surface tension is temperature dependent, meaning

$$S = S_0 + \frac{\partial S}{\partial T}\Delta T \tag{5.11}$$

(Koschmieder 1993, p. 37). We can keep the continuity equation, Eq. 5.1, the Navier-Stokes dynamical equation, Eq. 5.5 (although $-\alpha g T$ is now considered zero because fluid layers used for this convection are so exceptionally thin that significant differences in buoyancy between upper and lower fluid are not possible), and the thermal conduction equation, Eq. 5.8, that we developed for the Rayleigh-Benard case. When applying the boundary conditions of the system, the change in surface tension (due to temperature variations) is set equal to the shear stress at the upper surface. It is this shear stress that eventually sets the system into motion, because fluid is pulled *laterally* away from its position at the surface and must be replaced with fluid from below (Koschmieder 1993, p. 38).

Because surface tension theory neglects gravity, the Rayleigh number of the system is zero, and we must introduce a new control parameter to describe the system. The *Marangoni number* Ma is defined by

$$\mathrm{Ma} = \frac{\partial S}{\partial T}\frac{\Delta T d}{\rho \nu \kappa}, \tag{5.12}$$

and the critical value for the emergence of convection is $\mathrm{Ma}_{cr} = 79.607$ (Koschmieder 1993, p. 42). This critical value is a result of the same perturbations in velocity field and temperature (Eqs. 5.10a and 5.10b) that we introduced in the buoyancy driven case. As

before, these perturbations decay below the critical value in the control parameter and amplify above the critical value. Because this analysis neglects gravity, it is best applied to extremely thin layers of fluid. Buoyancy forces often dominate in thicker layers, and experimental work has shown that both driving forces are often present in a convective system (Koschmieder 1993, p. 37).

Chapter VI

Benard convection: experimentation and analysis

6.1 Experimentation

These experimental attempts closely followed the recommendations of Schatz and Van Hook (1997). Early attempts to produce convection cells were undertaken using a 'Handi-Pan' electric skillet and canola oil. Flow visualization was achieved by drying out gold-colored model paint and rinsing it with acetone; once dry again, small amounts of this residue were mixed with the oil. As predicted, the oil began at rest and convection cells appeared with sufficient temperature (see Fig. 6.1). The cells were mostly round and slightly non-uniform, so no further measurements were taken. Unfortunately, these early experiments were some of the most successful, as it soon became apparent that temperature is a difficult control parameter to work with.

The electric skillet did not provide very uniform heating, so a chemist's hot plate was used (Cimarec 2, Thermoclyne). It is exceptionally important that a uniform heat source be used. Using petri dishes to contain the fluid on the hot plate did not work because the slight convex shape of the bottom did not transfer heat evenly from the hot plate to the fluid. To create a more even heat source, I used a 1 cm thick piece of aluminum (high heat conductivity) as a lower boundary and created side walls using high temperature gasket sealant and PVC plastic. This was a much better heat source; the lower boundary temp was constant (as measured with the Fluke 52 thermocouple) between random points on the aluminum plate to within 0.5°C, yet the results were still marginal.

Using the recommendations of Schatz and Van Hook (1997), experiments were conducted using silicone oil of $\nu = 50$ cS and $\nu = 100$ cS with aluminum powder for visualization. The aluminum powder stays in suspension for a very limited amount of time, so it is quite difficult to slowly ramp the temperature and observe the onset of convection. When convection was reached, hexagonal patterns usually appeared, but

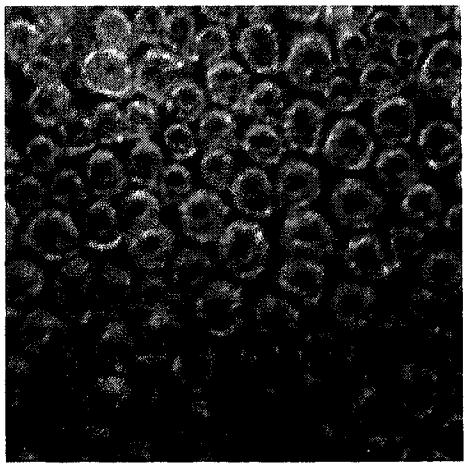

FIG. 6.1. Initial Marangoni-Benard convection results using a "Handi-Pan" and canola oil. Fluid thickness is about 1 cm.

these patterns were very faint (see Fig. 6.2a). Figure 6.2b shows the long, straight convection cells that also form. I was unable to find a gasket sealant that completely resisted the silicone oil, so the apparatus constantly leaked. Finally, when working with very thin layers, a level surface is essential, and it was rare that I achieved a fluid layer that was a constant thickness across the entire apparatus.

6.2 Measuring temperature and thickness

Convection was produced in the silicone oils and the canola oil over a range of thickness d from 2 mm to 10 mm, and the qualitative results were consistent with the predictions of Eq. 5.12. More temperature was always required for a smaller d, and hexagonal cells were often seen, although faint and non-uniform. Just as in the Taylor flow, the pattern wavelength was always similar to the size of the gap between boundaries, $\lambda \approx d$. While taking measurements with the thermocouple and a ruler, samples of canola oil of differing thickness were heated until the onset of convection, and these measurements are reported in Table 6.1. As shown by the definition of the Marangoni number in Eq. 5.12, the fluid thickness d and the temperature difference ΔT should be linearly proportional at the emergence of convection (i.e. at Ma_{cr}). The best-fit line of Fig. 6.3 demonstrates that the canola oil data fits this theory well.

6.3 Discussion

For simplicity, these experiments in convection were all under the assumption of a dominant surface-tension driving force. Although the examination of the onset of convection was less thorough than the study of the Taylor-Couette flow, the experiments were successful enough to verify the criticality of the phase transition to the unstable regime in a fluid heated from below. The experiments were also successful in illustrating the remarkable parallels between the Benard convection system and the Taylor-Couette system. If a more comprehensive study of Benard convection is undertaken by another thesis student, it will be essential to address immediately the problems of temperature

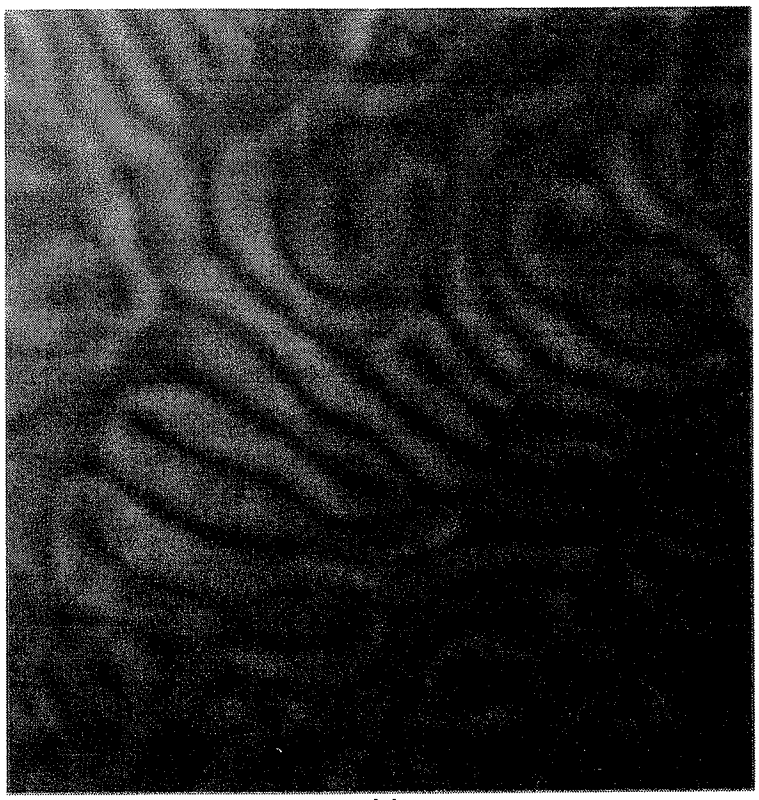

(a)

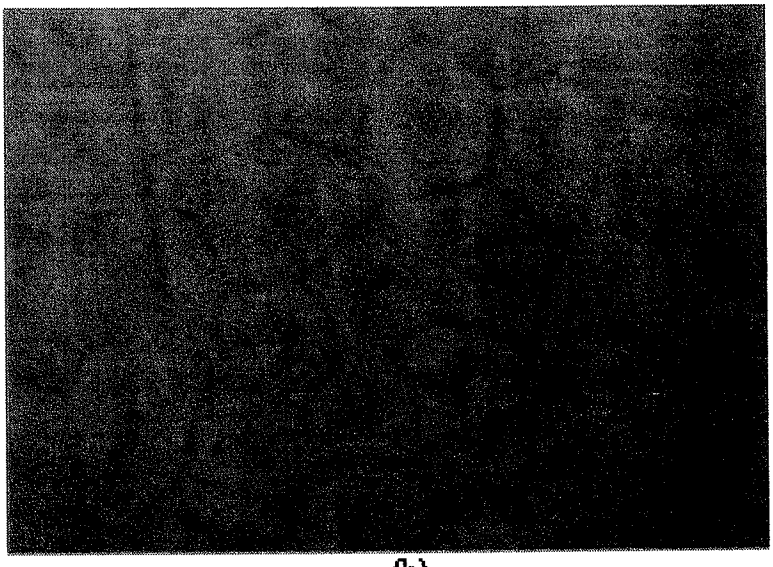

(b)

FIG. 6.2. Marangoni-Benard convection; (a) long convection cells in rheoscopic fluid and (b) hexagonal convection cells in silicone oil. Contrast enhanced using Adobe Photoshop.

TABLE 6.1. Measurements at the onset of convection in canola oil.

Fluid thickness d (cm)	Temperature difference ΔT (°C)
0.55 ± 0.05	17.5 ± 2
0.50 ± 0.05	19.0 ± 2
0.40 ± 0.05	28.5 ± 2
0.30 ± 0.05	35.5 ± 2

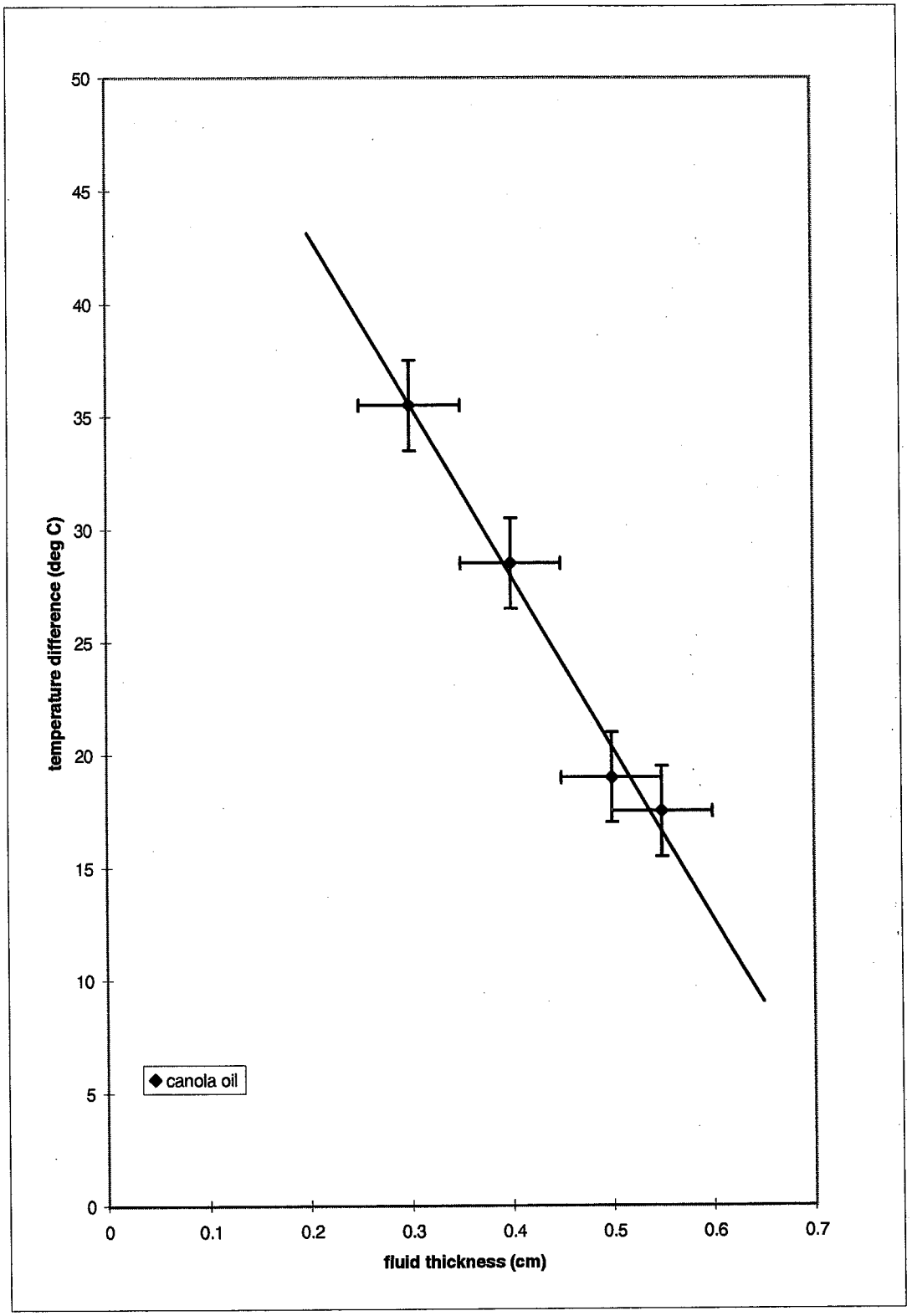

FIG. 6.3. Experimental verification of linear relationship between fluid thickness and temperature difference at the onset of surface-tension driven convection; solid line is a linear best-fit of the data.

control and flow visualization. Van Hook and Schatz suggest that aluminum flakes are best for visualization; perhaps the aluminum powder (spherical, diameter ~20 μm) I obtained from Sigma-Alderich Chemicals was inappropriate. However, I was unable to find any other fine aluminum powder from the major chemical supply companies. I believe that these experimental problems can be overcome; it would simply be a matter of time and concentrating solely on Benard convection.

Chapter VII
Conclusion

7.1 Discussion

This thesis has studied the fundamental properties of the emergence of Taylor vortices and Benard cells. Linear stability theory was verified experimentally for both cases, although admittedly, more thoroughly for the advent of Taylor vortices. Chandrasekhar's small gap approximation for Re_{cr} was also verified experimentally. Although Taylor-Couette flow and Benard convection are very different phenomena, the characteristics of the bifurcation point and the emergent complex flow were shown to be extremely similar. Both systems showed a phase transition to complex flow when a non-dimensional control parameter exceeded a critical value. In both cases, the pattern wavelength λ was similar in size to the distance between the boundaries of the flow. Although counter-intuitive, for both systems it was shown that the driving force necessary to reach complex flow patterns is actually smaller when the distance between boundaries was *increased.* These systems demonstrate the fundamental characteristics of emergent complexity.

7.2 Complexity, entropy, and "order for free"?

Although we developed a rather complete framework for understanding the onset of complexity in these flows, mystery still surrounds the emergence of complexity in simple systems. To the traditional scientist, emergent complexity is probably quite foreign and counter-intuitive; the second law of thermodynamics mandates that the universe should be moving towards simplicity, not complexity. Does the concept of increasing entropy not apply to these flows? Are these organized vortices and cells truly "order for free?" The answer is subtle. As demonstrated by numerous research groups, the emergence of complexity in these systems actually increases overall entropy

production (Goerner 1994, p. 87-91). Thus, the development of the organized, complex flows of Taylor vortices and Benard cells obeys the second law of thermodynamics and significantly hastens the entropy increase in the universe. In the aggregate, entropy still increases because the Benard cells are so much more effective at equalizing temperature (bringing hot to cold) than simple thermal diffusion, and the Taylor vortices are so much more effective than laminar flow at equalizing the sheer forces between boundaries. Again, we can take the implications far: can the evolution of complex and intelligent life be explained as a consequence of an, as yet, undiscovered law that complex structures arise because they maximize entropy production? Given the current rates at which humans utilize natural resources and produce disorder, the theory certainly seems suggestive, if not scientifically viable.

7.3 Suggestions for future work

The opportunities for future undergraduate research on this topic are nearly infinite. This thesis has only scratched the surface of the current body of knowledge surrounding the Taylor-Couette flow. The breadth of experimentation in this thesis was greatly limited by keeping the outer cylinder at rest ($\Omega_2 = 0$). However, it would be worthwhile to study the criticality of a number of other inner cylinder sizes (a_1) before altering the current apparatus to rotate the outer cylinder. If these additional inner cylinders were machined precisely, and if an electronic feed-back loop were implemented successfully to control the motor speed, it would be possible to both increase the precision of the results and to obtain a much more comprehensive examination of Re_{cr}. Other researchers have used laser-Doppler interferometry to measure the velocity of the flow at specific points in the vortices, and this should also be feasible at the undergraduate level. Alternatively, velocity might be measured by inserting dyes into various sections of the flow. By stabilizing the current apparatus mechanically, it should also be possible to drive the system at much higher angular speeds and thereby study the turbulent regime. Non linear stability theories have been developed to understand Taylor vortices; these theories would also be worth investigating.

The obvious suggestion for future work on Benard convection would be to construct an apparatus to study buoyancy driven, or Rayleigh-Benard, convection. This apparatus would require rigid boundaries of constant temperature above and below. The aluminum plate could still be used as the lower boundary; the real difficulty would be to create a transparent upper boundary so that the formation of convection cells could still be observed. Sapphire plates have been used by other researchers, but perhaps a cold water bath would be adequate. I was unable to obtain the thermal diffusivity or coefficient of expansion (from the CRC Handbook or from Sigma-Aldrich Chemical Company) for the silicone oils used; a thorough study of Ra_{cr} and Ma_{cr} could be undertaken by knowing these values. Non linear theories of both Rayleigh-Benard and Marangoni-Benard convection could be studied, as well the general theories for the case in which both driving forces are present.

I believe there is also extensive opportunity to explore further the philosophical implications and insights that Taylor vortices and Benard cells can provide as models of emergent complexity. The formation of these patterns is interesting in its own right, but it also seems that deep insights into the general mechanisms of evolving complexity can be gleaned from these simple phenomena. What are the fundamental laws of physics and properties of matter that cause complexity to emerge in systems of all kinds (including living), and how can these two experiments lead us to a better understanding of ourselves as complex natural systems?

REFERENCES

Chandrasekhar, S. *Hydrodynamic and Hydromagnetic Stability.* New York: Dover Publications, Inc., 1961.

Couette, M.M. *Ann. Chim. Physics,* Ser. VI 21, 1890.

Donnelly, Russel J. "Taylor-Couette Flow: the Early Days." *Physics Today.* 1991, Volume 44, November, pp. 33-40.

Fauve, A., Gritton, H., Gritton, J., Lichnerowicy, A., and Wolf, E. *Chaos and Determinism: Turbulence as a Paradigm for Complex Systems Converging Towards Final States.* Balitmore: Johns Hopkins University Press, 1995.

Gleick, J. *Chaos.* New York: Viking Press, 1992.

Goerner, S.J. *Chaos and the Ecological Universe.* Amsterdam: Gordon and Breach Science Publishers, 1994.

Griffiths, D.J. *Introduction to Electrodynamics, 2nd ed.* Englewood Cliffs, New Jersey: Prentice-Hall, Inc., 1989.

Ho, M.W. *The Rainbow and the Worm: the Physics of Organisms.* New Jersey: World Scientific Publishing Co., 1998.

Kauffman, S. *At Home in the Universe.* New York: Oxford University Press, 1995.

Kobine, J. J., Mullin, T. "Low Dimensional Bifurcation Phenomena in Taylor-Couette Flow with Discrete Azimuthal Symmetry." *Journal of Fluid Mechanics.* 1994, Volume 275, pp. 379-405.

Koschmieder, E.L. *Benard Cells and Taylor Vorticies*. New York: Cambridge University Press, 1993.

Landau, L. D., Lifshitz, E. M. *Fluid Mechanics*. New York: Pergamon Press, 1987.

Newton, I. *Mathematical Principles*. Cajori, F., ed. Berkeley: U. California Press, 1946.

Prakash, A., and Koster, J. N. "Steady Rayleigh-Benard Convection in a Two-Layer System of Immiscible Liquids." *Journal of Heat Transfer*. 1996, Volume 118, pp. 366-373.

Schatz, M. F., and Van Hook, S. J. "Simple Demonstrations of Pattern Formation." *The Physics Teacher*. 1997, Volume 35, pp. 391-395.

Sears, F.W. and Zemansky, M.W. *College Physics*. Reading, Massachusetts: Addison-Wesley Publishing Company, Inc., 1960.

Stokes, G.G. *Mathematical and Physical Papers*, vol. 1. Cambridge, England: Cambridge U. Press, 1880.

Symon, Keith R. *Mechanics, 3rd ed.* Reading, Massachusetts: Addison-Wesley Publishing Company, 1971.

Tagg, R. "A Guide to Literature Related to the Taylor-Couette Problem." *Ordered and Turbulent Patterns in the Taylor-Couette Flow*. Andereck, C.D. and Hayot, F., eds. New York: Plenum, 1992, pp. 303-354.

Tagg, R. "Instabilities and the Origin of Complexity in Fluid Flows." *1993 Lectures in Complex Systems*. Nadel, L. and Stein, D.L., eds. Reading, Massachusetts: Addison-Wesley Publishing Company, Inc., 1995.

Taylor, G.I. *Philosophical Transactions of the Royal Society of London,* Ser. A 233, 1923.

Tritton, D. J. *Physical Fluid Dynamics*. New York: Oxford University Press, 1988.

Young, H.D. *Statistical Treatment of Experimental Data*. New York: McGraw-Hill, 1962.

Weisshaar, E., Busse, F. H., and Nagata, M. "Twist Vortices and their Instabilities in the Taylor-Couette System." *Journal of Fluid Mechanics.* 1991, Volume 226, pp. 549-564.

Appendix A:
Taylor-Couette data

Appendix A, Viscosity of Solutions

Solution # 2		Solution # 3		Solution # 1		Solution # 4	
Fluid: 50/50 glycerol / water		**Fluid:** 50/50 by volume		**Fluid:** 40/60 glycerol / water		**Fluid:** 65/35 glycerol / water	
Density (g/ml)	1.104	Density (g/ml)	1.118	Density (g/ml)	1.079	Density (g/ml)	1.150
Density (g/ml)	1.110	Density (g/ml)	1.127	Density (g/ml)	1.082	Density (g/ml)	1.156
Density (g/ml)	1.106	Density (g/ml)	1.119	Density (g/ml)	1.079	Density (g/ml)	1.154
avg=	**1.107** g/ml	Density (g/ml)	1.129	avg=	**1.080** g/ml	Density (g/ml)	1.156
stdev=	0.0031 g/ml	avg=	**1.123** g/ml	stdev=	0.0016 g/ml	avg=	**1.154** g/ml
%stdev=	0.28%	stdev=	0.0057 g/ml	%stdev=	0.15%	stdev=	0.0028 g/ml
		%stdev=	0.51%			%stdev=	0.25%
+/-	0.0057 g/ml	+/-	0.0058 g/ml	+/-	0.0056 g/ml	+/-	0.0059 g/ml
Viscosity (cS)	5.08	Viscosity (cS)	8.52	Viscosity (cS)	3.41	Viscosity (cS)	11.86
Viscosity (cS)	5.03	Viscosity (cS)	8.49	Viscosity (cS)	3.45	Viscosity (cS)	12.29
Viscosity (cS)	5.24	Viscosity (cS)	8.54	Viscosity (cS)	3.39	Viscosity (cS)	12.58
Viscosity (cS)	5.40	Viscosity (cS)	8.50	Viscosity (cS)	3.47	Viscosity (cS)	12.58
Viscosity (cS)	5.39	Viscosity (cS)	8.42	Viscosity (cS)	3.44	Viscosity (cS)	12.63
Viscosity (cS)	5.21	Viscosity (cS)	8.43	Viscosity (cS)	3.41	Viscosity (cS)	12.34
Viscosity (cS)	5.05	Viscosity (cS)	8.50	Viscosity (cS)	3.29	Viscosity (cS)	12.30
Viscosity (cS)	5.15	Viscosity (cS)	8.38	Viscosity (cS)	3.36	Viscosity (cS)	12.13
Viscosity (cS)	5.37	Viscosity (cS)	8.96	Viscosity (cS)	3.36	Viscosity (cS)	12.34
Viscosity (cS)	5.43	Viscosity (cS)	8.86	Viscosity (cS)	3.24	Viscosity (cS)	12.22
Viscosity (cS)	5.39	Viscosity (cS)	8.80	Viscosity (cS)	3.26	Viscosity (cS)	11.94
Viscosity (cS)	5.16	Viscosity (cS)	8.95	Viscosity (cS)	3.35	Viscosity (cS)	12.08
Viscosity (cS)	5.43	Viscosity (cS)	8.86	Viscosity (cS)	3.37	Viscosity (cS)	12.16
Viscosity (cS)	5.36	Viscosity (cS)	8.76	Viscosity (cS)	3.25	Viscosity (cS)	12.25
Viscosity (cS)	5.17	Viscosity (cS)	8.78236	Viscosity (cS)	3.25	Viscosity (cS)	12.29
avg=	**5.26** cS	avg=	**8.65** cS	avg=	**3.35** cS	avg=	**12.27** cS
stdev=	0.147 cS	stdev=	0.208 cS	stdev=	0.077 cS	stdev=	0.221 cS
%stdev=	2.80%	%stdev=	2.41%	%stdev=	2.30%	%stdev=	1.81%
+/-	0.079851 cS	+/-	0.100634 cS	+/-	0.072988 cS	+/-	0.130058 cS

Appendix A, Solution # 1

Fluid: 40:60 glycercol / water (by mass)

Large A1 Re(theoretical)= 95.24

Run #1		**Run #2**		**Run #3**		**Run #4**		**Run #5**	
Signal (kHz)	Omega (rad/s)	Signal (kHz)	Omega (rad/s)	Signal (kHz)	Omega (rad/s)	Signal (kHz)	Omega (rad/s)	Signal (kHz)	Omega (rad/s)
5.21	1.000	5.04	0.967	5.31	1.019	5.43	1.042	4.75	0.911
5.19	0.996	5.26	1.009	5.32	1.021	5.35	1.026	5.17	0.992
4.98	0.955	5.11	0.980	5.17	0.992	4.99	0.957	5.00	0.959
5.16	0.990	4.79	0.919	5.07	0.973	5.48	1.051	5.05	0.969
5.14	0.986	5.29	1.015	5.34	1.024	5.15	0.988	5.09	0.977
5.24	1.005	5.14	0.986	5.22	1.001	5.57	1.069	5.25	1.007
5.21	1.000	4.75	0.911	5.02	0.963	5.25	1.007	4.89	0.938
4.80	0.921	4.79	0.919	5.25	1.007	5.22	1.001	4.76	0.913
5.17	0.992	4.72	0.906	5.13	0.984	5.17	0.992	4.83	0.927
5.30	1.017	4.90	0.940	5.27	1.011	5.13	0.984	4.67	0.896
5.35	1.026	5.41	1.038	5.22	1.001	5.38	1.032	5.19	0.996
5.56	1.067	5.36	1.028	4.84	0.929	5.20	0.998	4.83	0.927
5.38	1.032	5.27	1.011	4.79	0.919	5.38	1.032	4.77	0.915
4.95	0.950	5.15	0.988	5.17	0.992	5.09	0.977	5.03	0.965
5.17	0.992	5.14	0.986	5.08	0.975	5.12	0.982	4.71	0.904
5.39	1.034	5.29	1.015	5.23	1.003	5.31	1.019	4.79	0.919
5.34	1.024	4.67	0.896	5.29	1.015	5.38	1.032	4.92	0.944
5.07	0.973	5.13	0.984	5.55	1.065	5.17	0.992	4.68	0.898
5.28	1.013	5.29	1.015	5.47	1.049	5.19	0.996	5.14	0.986
5.07	0.973	4.68	0.898	4.92	0.944	5.40	1.036	4.67	0.896
avg=	0.997	avg=	0.971	avg=	0.994	avg=	1.011	avg=	0.942
stdev=	0.033	stdev=	0.047	stdev=	0.037	stdev=	0.029	stdev=	0.037
%stdev=	3.33%	%stdev=	4.89%	%stdev=	3.70%	%stdev=	2.83%	%stdev=	3.89%

5 runs:

avg. omega= 0.983 rad/s
stdev= 0.02712 rad/s
%stdev= 2.76%

pattern thickness *d*= 0.085cm +/- 0.05cm

m =/= 0 at *omega* = 1.765 rad/s

Re(experimental) = 103.14 +/- 0.15453241
% diff (exp. to th.)= 8.30%

Fluid: 40:60 glycerol/water (by mass)

Small A1 Re(theoretical)= 84.06

Run #1		**Run #2**		**Run #3**		**Run #4**		**Run #5**	
Signal (kHz)	Omega (rad/s)	Signal (kHz)	Omega (rad/s)	Signal (kHz)	Omega (rad/s)	Signal (kHz)	Omega (rad/s)	Signal (kHz)	Omega (rad/s)
3.86	0.741	3.53	0.677	4.47	0.858	4.12	0.790	3.71	0.712
3.47	0.666	3.67	0.704	4.01	0.769	4.18	0.802	3.94	0.756
3.87	0.742	3.41	0.654	4.09	0.785	4.08	0.783	4.03	0.773
3.64	0.698	3.50	0.671	4.26	0.817	3.79	0.727	3.94	0.756
3.81	0.731	3.45	0.662	4.34	0.833	4.29	0.823	4.11	0.789
3.63	0.696	3.95	0.758	4.30	0.825	3.94	0.756	3.99	0.765
3.74	0.718	4.18	0.802	3.99	0.765	4.08	0.783	3.80	0.729
4.00	0.767	4.20	0.806	4.37	0.838	3.72	0.714	4.17	0.800
3.68	0.706	3.81	0.731	4.24	0.813	4.02	0.771	3.83	0.735
3.48	0.668	4.25	0.815	4.33	0.831	3.94	0.756	4.22	0.810
3.97	0.762	4.23	0.812	4.18	0.802	3.91	0.750	4.16	0.798
3.37	0.647	3.90	0.748	4.20	0.806	4.13	0.792	3.80	0.729
3.82	0.733	4.01	0.769	4.33	0.831	4.20	0.806	3.88	0.744
3.72	0.714	3.98	0.764	4.53	0.869	3.69	0.708	4.21	0.808
3.50	0.671	3.37	0.647	4.06	0.779	4.02	0.771	3.86	0.741
4.19	0.804	3.58	0.687	4.01	0.769	3.80	0.729	4.24	0.813
3.65	0.700	3.70	0.710	4.42	0.848	3.81	0.731	3.94	0.756
3.66	0.702	3.42	0.656	4.13	0.792	3.99	0.765	3.72	0.714
3.30	0.633	3.95	0.758	4.09	0.785	4.10	0.787	3.86	0.741
3.76	0.721	4.23	0.812	4.00	0.767	3.87	0.742	4.07	0.781
avg=	0.711	avg=	0.732	avg=	0.809	avg=	0.763	avg=	0.762
stdev=	0.042	stdev=	0.060	stdev=	0.032	stdev=	0.032	stdev=	0.032
%stdev=	5.91%	%stdev=	8.17%	%stdev=	3.95%	%stdev=	4.25%	%stdev=	4.26%

5 runs:

avg. *omega*= 0.756 rad/s
stdev= 0.037107 rad/s
%stdev= 4.91%

pattern thickness *d*= 1.05cm +/- 0.05cm

m =/= 0 at *omega* = 3.453 rad/s

Re(experimental) = 79.28 +/- 0.11479974
% diff (exp. to th.)= 5.69%

Appendix A, Solution # 2

Fluid: 50:50 glycercol / water (by mass)

Large A1 Re(theoretical)= 95.24

Run #1		**Run #2**		**Run #3**		**Run #4**		**Run #5**	
Signal (kHz)	Omega (rad/s)	Signal (kHz)	Omega (rad/s)	Signal (kHz)	Omega (rad/s)	Signal (kHz)	Omega (rad/s)	Signal (kHz)	Omega (rad/s)
7.50	1.439	8.15	1.564	7.11	1.364	7.40	1.420	7.16	1.374
7.19	1.379	7.47	1.433	7.14	1.370	7.54	1.447	7.91	1.518
7.92	1.519	8.14	1.562	7.50	1.439	7.98	1.531	7.88	1.512
7.29	1.399	7.68	1.473	7.15	1.372	7.59	1.456	7.49	1.437
7.76	1.489	7.17	1.376	7.25	1.391	7.15	1.372	7.74	1.485
7.45	1.429	7.64	1.466	7.42	1.424	7.21	1.383	7.95	1.525
7.89	1.514	8.28	1.589	7.13	1.368	7.49	1.437	7.66	1.470
7.34	1.408	7.34	1.408	8.18	1.569	7.49	1.437	7.67	1.472
7.46	1.431	7.97	1.529	7.05	1.353	7.25	1.391	8.14	1.562
7.98	1.531	7.34	1.408	8.13	1.560	8.18	1.569	7.32	1.404
7.66	1.470	7.09	1.360	7.12	1.366	7.49	1.437	7.06	1.354
7.51	1.441	7.68	1.473	6.77	1.299	7.55	1.448	7.11	1.364
7.03	1.349	7.77	1.491	7.16	1.374	7.81	1.498	7.50	1.439
7.89	1.514	7.20	1.381	7.10	1.362	7.73	1.483	7.14	1.370
7.40	1.420	7.51	1.441	7.22	1.385	7.85	1.506	7.21	1.383
7.06	1.354	7.54	1.447	7.60	1.458	7.86	1.508	7.41	1.422
7.57	1.452	7.89	1.514	7.95	1.525	7.71	1.479	7.89	1.514
7.23	1.387	8.01	1.537	7.88	1.512	7.23	1.387	8.02	1.539
7.73	1.483	7.54	1.447	7.84	1.504	7.10	1.362	7.71	1.479
7.27	1.395	7.50	1.439	8.01	1.537	7.83	1.502	7.32	1.404
avg=	1.440	avg=	1.467	avg=	1.427	avg=	1.453	avg=	1.451
stdev=	0.055	stdev=	0.066	stdev=	0.081	stdev=	0.057	stdev=	0.065
%stdev=	3.84%	%stdev=	4.48%	%stdev=	5.65%	%stdev=	3.91%	%stdev=	4.47%

5 runs:

avg. omega= 1.447 rad/s

stdev= 0.01507 rad/s

%stdev= 1.04%

pattern thickness *d*= 0.085cm +/- 0.05cm

m =/= 0 at *omega* = 2.014 rad/s

Re(experimental) = 96.91 +/- 0.13538855

% diff (exp. to th.)= 1.75%

Appendix A, Solution # 2

Fluid: 50:50 glycerol/water (by mass)

Small A1 Re(theoretical)= 84.06

Run #1		**Run #2**		**Run #3**		**Run #4**		**Run #5**	
Signal (kHz)	Omega (rad/s)	Signal (kHz)	Omega (rad/s)	Signal (kHz)	Omega (rad/s)	Signal (kHz)	Omega (rad/s)	Signal (kHz)	Omega (rad/s)
5.95	1.142	5.88	1.128	5.38	1.032	5.56	1.067	5.99	1.149
5.91	1.134	5.62	1.078	5.40	1.036	5.50	1.055	5.42	1.040
5.85	1.122	5.72	1.097	5.23	1.003	5.86	1.124	5.39	1.034
5.70	1.094	5.94	1.140	5.65	1.084	5.69	1.092	6.04	1.159
6.03	1.157	5.90	1.132	5.30	1.017	6.05	1.161	5.92	1.136
5.76	1.105	5.47	1.049	5.64	1.082	5.82	1.117	5.86	1.124
5.79	1.111	5.60	1.074	5.53	1.061	5.76	1.105	5.56	1.067
5.48	1.051	5.56	1.067	5.76	1.105	5.64	1.082	5.88	1.128
5.37	1.030	5.66	1.086	6.09	1.168	5.75	1.103	5.79	1.111
5.54	1.063	5.79	1.111	5.60	1.074	5.54	1.063	5.17	0.992
5.63	1.080	5.80	1.113	5.53	1.061	5.44	1.044	5.23	1.003
5.36	1.028	5.18	0.994	5.74	1.101	6.02	1.155	5.53	1.061
5.91	1.134	5.92	1.136	5.94	1.140	5.85	1.122	5.42	1.040
5.88	1.128	5.99	1.149	5.70	1.094	5.69	1.092	5.87	1.126
5.68	1.090	5.53	1.061	5.53	1.061	5.46	1.048	5.33	1.023
5.88	1.128	5.41	1.038	5.94	1.140	5.20	0.998	5.87	1.126
5.68	1.090	5.84	1.120	5.48	1.051	5.43	1.042	5.83	1.119
5.67	1.088	5.85	1.122	5.26	1.009	5.50	1.055	5.50	1.055
5.31	1.019	5.93	1.138	5.95	1.142	5.73	1.099	5.43	1.042
5.99	1.149	5.26	1.009	5.78	1.109	5.86	1.124	5.53	1.061
avg=	1.097	avg=	1.092	avg=	1.079	avg=	1.088	avg=	1.080
stdev=	0.042	stdev=	0.045	stdev=	0.047	stdev=	0.042	stdev=	0.051
%stdev=	3.79%	%stdev=	4.11%	%stdev=	4.35%	%stdev=	3.86%	%stdev=	4.77%

5 runs:

avg. *omega*= 1.087 rad/s

stdev= 0.007986 rad/s

%stdev= 0.73%

pattern thickness *d*= 1.05cm +/- 0.05cm

m =/= 0 at *omega* = 4.298 rad/s

Re(experimental) = 72.79 +/- 0.10015415

% diff (exp. to th.)= 13.41%

Appendix A, Solution # 3

Fluid: Solution X, aprox. 50:50 glycercol / water (by volume)

Large A1 Re(theoretical)= 95.24

Run #1		**Run #2**		**Run #3**		**Run #4**		**Run #5**	
Signal (kHz)	Omega (rad/s)	Signal (kHz)	Omega (rad/s)	Signal (kHz)	Omega (rad/s)	Signal (kHz)	Omega (rad/s)	Signal (kHz)	Omega (rad/s)
12.98	2.490	13.18	2.529	12.82	2.460	13.08	2.509	12.90	2.475
12.74	2.444	13.25	2.542	12.91	2.477	13.00	2.494	12.81	2.458
12.95	2.484	12.99	2.492	12.69	2.435	12.97	2.488	13.04	2.502
13.21	2.534	13.01	2.496	12.87	2.469	12.99	2.492	13.00	2.494
12.99	2.492	13.11	2.515	13.09	2.511	13.06	2.506	12.96	2.486
13.17	2.527	13.03	2.500	12.94	2.483	12.88	2.471	13.15	2.523
13.02	2.498	13.05	2.504	13.23	2.538	12.99	2.492	13.14	2.521
13.23	2.538	13.19	2.531	12.90	2.475	12.79	2.454	13.03	2.500
13.10	2.513	13.08	2.509	13.14	2.521	12.80	2.456	12.93	2.481
13.09	2.511	13.01	2.496	13.12	2.517	12.66	2.429	13.07	2.508
13.87	2.661	13.00	2.494	12.89	2.473	12.78	2.452	13.06	2.506
13.10	2.513	13.11	2.515	12.79	2.454	12.98	2.490	13.04	2.502
13.01	2.496	13.24	2.540	12.86	2.467	12.88	2.471	13.11	2.515
13.11	2.515	13.21	2.534	12.85	2.465	12.95	2.484	12.91	2.477
13.25	2.542	12.89	2.473	12.81	2.458	12.88	2.471	12.90	2.475
12.85	2.465	13.16	2.525	13.18	2.529	12.91	2.477	13.08	2.509
13.00	2.494	12.78	2.452	12.94	2.483	12.79	2.454	12.89	2.473
12.90	2.475	13.30	2.552	13.13	2.519	13.00	2.494	13.17	2.527
12.98	2.490	13.12	2.517	12.97	2.488	12.99	2.492	13.07	2.508
13.12	2.517	13.17	2.527	12.97	2.488	12.85	2.465	13.19	2.531
avg=	2.510	avg=	2.512	avg=	2.485	avg=	2.477	avg=	2.498
stdev=	0.043	stdev=	0.024	stdev=	0.028	stdev=	0.021	stdev=	0.020
%stdev=	1.72%	%stdev=	0.98%	%stdev=	1.13%	%stdev=	0.84%	%stdev=	0.82%

5 runs:

avg. omega= 2.497 rad/s
stdev= 0.01525 rad/s
%stdev= 0.61%

pattern thickness *d*= 0.085cm +/- 0.05cm

m =/= 0 at *omega* = 3.262 rad/s

Re(experimental) = 101.59 +/- 0.13459067
% diff (exp. to th.)= 6.67%

Appendix A, Solution # 3

Fluid: Solution X, aprox. 50:50 glycerol/water (by volume)

Small A1 Re(theoretical)= 84.06

Run #1		**Run #2**		**Run #3**		**Run #4**		**Run #5**	
Signal (kHz)	Omega (rad/s)	Signal (kHz)	Omega (rad/s)	Signal (kHz)	Omega (rad/s)	Signal (kHz)	Omega (rad/s)	Signal (kHz)	Omega (rad/s)
9.44	1.811	9.91	1.901	9.66	1.853	9.95	1.909	9.58	1.838
9.83	1.886	9.66	1.853	9.86	1.892	9.88	1.896	9.69	1.859
9.79	1.878	9.74	1.869	9.83	1.886	9.57	1.836	9.72	1.865
9.85	1.890	9.71	1.863	9.83	1.886	9.85	1.890	9.72	1.865
9.69	1.859	9.84	1.888	9.72	1.865	9.79	1.878	9.50	1.823
9.65	1.851	9.59	1.840	9.67	1.855	9.62	1.846	9.68	1.857
9.72	1.865	9.65	1.851	9.64	1.849	9.81	1.882	9.72	1.865
9.77	1.874	9.79	1.878	9.67	1.855	9.62	1.846	9.79	1.878
9.75	1.871	9.76	1.872	9.62	1.846	9.93	1.905	9.67	1.855
9.67	1.855	9.60	1.842	9.49	1.821	9.62	1.846	9.68	1.857
9.57	1.836	9.65	1.851	9.50	1.823	9.60	1.842	9.72	1.865
9.57	1.836	9.78	1.876	9.68	1.857	9.66	1.853	9.62	1.846
9.54	1.830	9.74	1.869	9.50	1.823	9.84	1.888	9.79	1.878
9.85	1.890	9.58	1.838	9.60	1.842	9.77	1.874	9.56	1.834
9.80	1.880	9.83	1.886	9.37	1.798	9.78	1.876	9.75	1.871
9.69	1.859	9.64	1.849	9.43	1.809	9.85	1.890	9.63	1.848
9.79	1.878	9.57	1.836	9.37	1.798	9.82	1.884	9.55	1.832
9.70	1.861	9.77	1.874	9.54	1.830	9.69	1.859	9.81	1.882
9.70	1.861	9.84	1.888	9.86	1.892	9.57	1.836	9.74	1.869
9.77	1.874	9.89	1.897	9.64	1.849	9.59	1.840	9.57	1.836
avg=	1.862	avg=	1.866	avg=	1.846	avg=	1.867	avg=	1.856
stdev=	0.021	stdev=	0.020	stdev=	0.029	stdev=	0.023	stdev=	0.017
%stdev=	1.13%	%stdev=	1.08%	%stdev=	1.58%	%stdev=	1.23%	%stdev=	0.91%

5 runs:

avg. *omega*= 1.860 rad/s

stdev= 0.008463 rad/s

%stdev= 0.46%

pattern thickness *d*= 1.05cm +/- 0.05cm

m =/= 0 at *omega* = 6.71145 rad/s

Re(experimental) = 75.66 +/- 0.09971714

% diff (exp. to th.)= 9.99%

Appendix A, Solution # 4

Fluid: 65:35 glycercol / water (by mass)

Large A1 Re(theoretical)= 95.24

Run #1		**Run #2**		**Run #3**		**Run #4**		**Run #5**	
Signal (kHz)	Omega (rad/s)	Signal (kHz)	Omega (rad/s)	Signal (kHz)	Omega (rad/s)	Signal (kHz)	Omega (rad/s)	Signal (kHz)	Omega (rad/s)
17.99	3.451	17.95	3.444	18.06	3.465	17.87	3.428	17.89	3.432
17.75	3.405	18.02	3.457	17.97	3.448	17.72	3.400	17.86	3.426
17.97	3.448	17.96	3.446	17.86	3.426	17.92	3.438	17.85	3.425
17.91	3.436	17.91	3.436	17.97	3.448	17.78	3.411	17.98	3.450
17.87	3.428	17.98	3.450	18.07	3.467	18.00	3.453	17.74	3.403
17.94	3.442	17.87	3.428	18.01	3.455	17.87	3.428	17.89	3.432
17.85	3.425	18.03	3.459	18.27	3.505	17.78	3.411	17.81	3.417
17.98	3.450	18.01	3.455	18.15	3.482	17.80	3.415	17.69	3.394
17.89	3.432	17.96	3.446	17.83	3.421	17.82	3.419	17.85	3.425
17.63	3.382	17.97	3.448	17.92	3.438	17.79	3.413	17.93	3.440
17.87	3.428	17.85	3.425	17.86	3.426	17.83	3.421	17.93	3.440
17.88	3.430	18.07	3.467	18.04	3.461	17.81	3.417	17.89	3.432
17.83	3.421	18.02	3.457	17.98	3.450	17.85	3.425	17.75	3.405
18.08	3.469	17.93	3.440	17.87	3.428	18.06	3.465	17.83	3.421
17.85	3.425	18.06	3.465	17.85	3.425	17.95	3.444	17.84	3.423
17.98	3.450	17.93	3.440	17.89	3.432	17.71	3.398	17.90	3.434
17.98	3.450	18.28	3.507	18.00	3.453	17.86	3.426	17.85	3.425
17.94	3.442	18.01	3.455	17.83	3.421	17.87	3.428	17.81	3.417
17.91	3.436	17.99	3.451	18.10	3.473	17.78	3.411	17.79	3.413
17.85	3.425	17.86	3.426	17.99	3.451	17.90	3.434	17.97	3.448
avg=	3.434	avg=	3.450	avg=	3.449	avg=	3.424	avg=	3.425
stdev=	0.019	stdev=	0.018	stdev=	0.022	stdev=	0.017	stdev=	0.014
%stdev=	0.54%	%stdev=	0.52%	%stdev=	0.65%	%stdev=	0.49%	%stdev=	0.42%

5 runs:

avg. omega= 3.436 rad/s
stdev= 0.01248 rad/s
%stdev= 0.36%

pattern thickness *d*= 0.085cm +/- 0.05cm

m =/= 0 at *omega* = 4.988 rad/s

Re(experimental) = 98.62 +/- 0.12730158
% diff (exp. to th.)= 3.55%

Appendix A, Solution # 4

Fluid: 65:35 glycerol/water (by mass)

Small A1 Re(theoretical)= 84.06

Run #1		**Run #2**		**Run #3**		**Run #4**		**Run #5**	
Signal (kHz)	Omega (rad/s)	Signal (kHz)	Omega (rad/s)	Signal (kHz)	Omega (rad/s)	Signal (kHz)	Omega (rad/s)	Signal (kHz)	Omega (rad/s)
13.36	2.563	13.13	2.519	13.61	2.611	13.61	2.611	13.46	2.582
13.28	2.548	13.11	2.515	13.46	2.582	13.56	2.602	13.42	2.575
13.33	2.557	13.30	2.552	13.33	2.557	13.40	2.571	13.39	2.569
13.41	2.573	13.32	2.555	13.59	2.607	13.40	2.571	13.38	2.567
13.29	2.550	13.20	2.532	13.45	2.580	13.52	2.594	13.33	2.557
13.27	2.546	13.29	2.550	13.56	2.602	13.50	2.590	13.36	2.563
13.32	2.555	13.26	2.544	13.49	2.588	13.56	2.602	13.61	2.611
13.34	2.559	13.35	2.561	13.68	2.625	13.42	2.575	13.45	2.580
13.44	2.579	13.35	2.561	13.39	2.569	13.42	2.575	13.38	2.567
13.33	2.557	13.29	2.550	13.43	2.577	13.51	2.592	13.57	2.603
13.24	2.540	13.15	2.523	13.46	2.582	13.43	2.577	13.41	2.573
13.49	2.588	13.30	2.552	13.62	2.613	13.36	2.563	13.29	2.550
13.43	2.577	13.46	2.582	13.62	2.613	13.33	2.557	13.49	2.588
13.46	2.582	13.18	2.529	13.50	2.590	13.26	2.544	13.37	2.565
13.33	2.557	13.31	2.554	13.33	2.557	13.27	2.546	13.43	2.577
13.37	2.565	13.22	2.536	13.49	2.588	13.31	2.554	13.41	2.573
13.39	2.569	13.36	2.563	13.63	2.615	13.42	2.575	13.52	2.594
13.50	2.590	13.40	2.571	13.50	2.590	13.32	2.555	13.42	2.575
13.53	2.596	13.38	2.567	13.45	2.580	13.45	2.580	13.33	2.557
13.32	2.555	13.29	2.550	13.44	2.579	13.45	2.580	13.37	2.565
avg=	2.565	avg=	2.548	avg=	2.590	avg=	2.574	avg=	2.575
stdev=	0.016	stdev=	0.018	stdev=	0.019	stdev=	0.017	stdev=	0.015
%stdev=	0.61%	%stdev=	0.70%	%stdev=	0.74%	%stdev=	0.68%	%stdev=	0.60%

5 runs:

avg. *omega*= 2.570 rad/s

stdev= 0.015323 rad/s

%stdev= 0.60%

pattern thickness *d*= 1.05cm +/- 0.05cm

m =/= 0 at *omega* = 5.765 rad/s

Re(experimental) = 73.77 +/- 0.09520212

% diff (exp. to th.)= 12.24%

Appendix B:
Taylor-Couette images

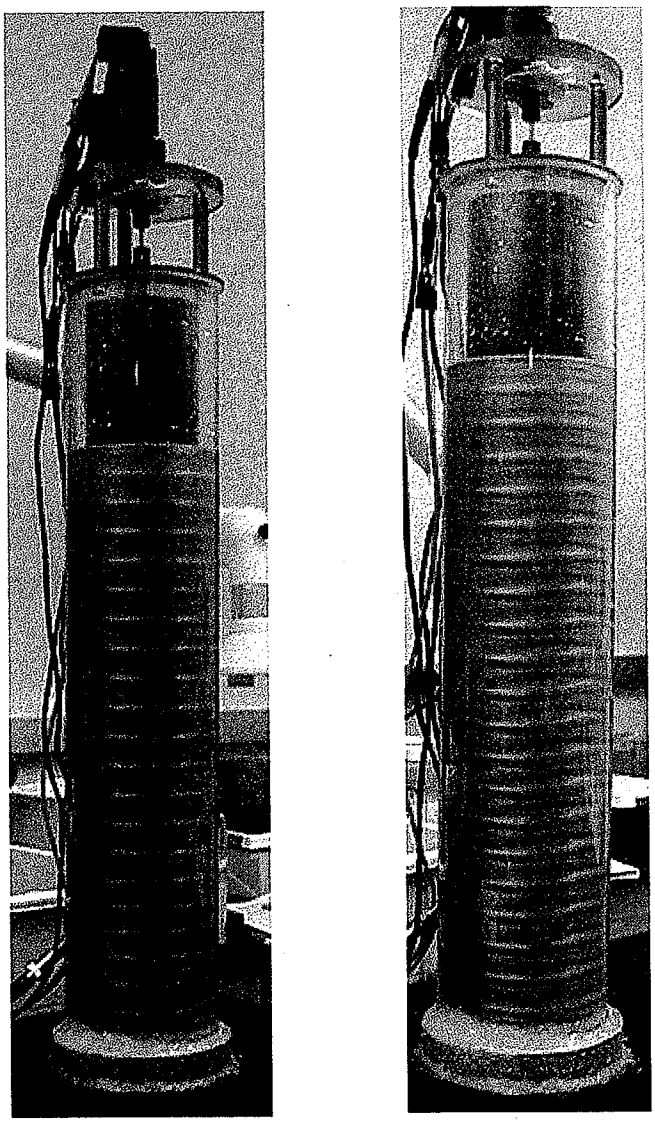

(a) (b)

FIG. B.8. Supercritical flow using Solution #4 (composition 65:35 glycerol:water, by mass) and the small inner cylinder (a1 = 4.22 cm). (a) Taylor vortices; (b) wavy Taylor vortices.

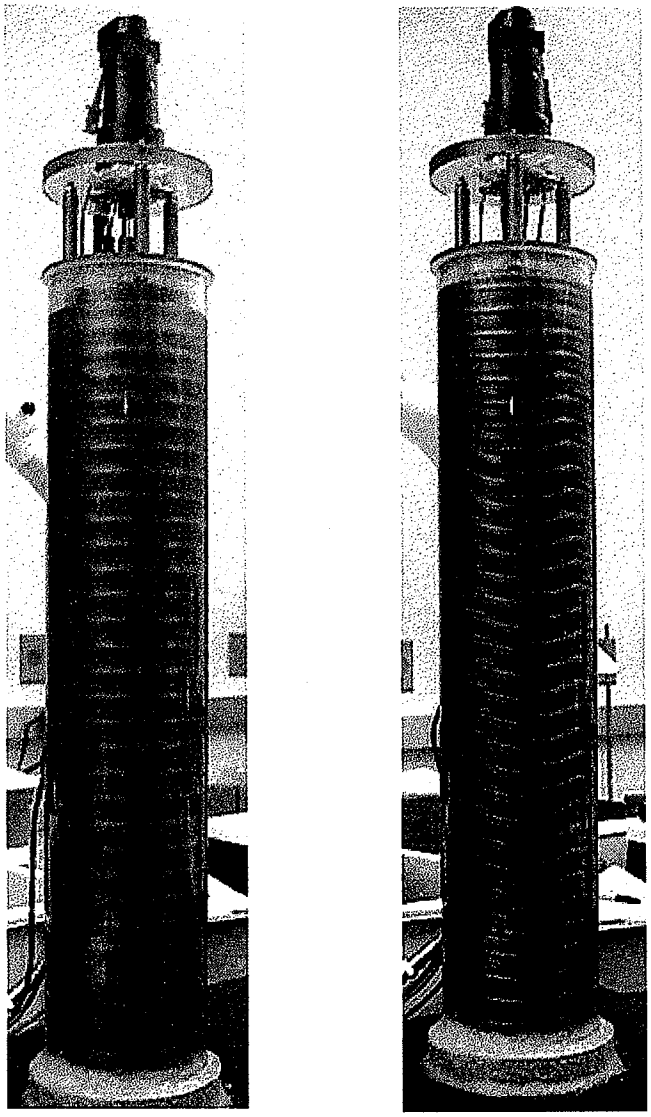

(a) (b)

FIG. B.7. Supercritical flow using Solution #4 (composition 65:35 glycerol:water, by mass) and the large inner cylinder (a1 = 4.44 cm). (a) Taylor vortices; (b) wavy Taylor vortices.

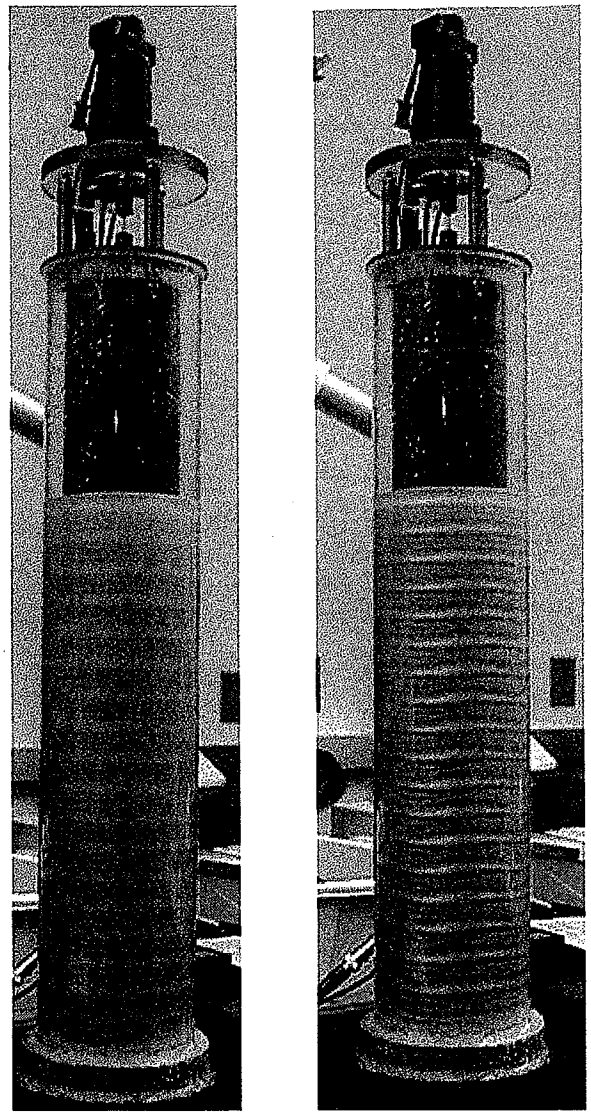

(a) (b)

FIG. B.6. Supercritical flow using Solution # 3 (composition 50:50 glycerol:water, by volume) and the small inner cylinder (a1 = 4.22 cm). (a) Taylor vortices; (b) wavy Taylor vortices.

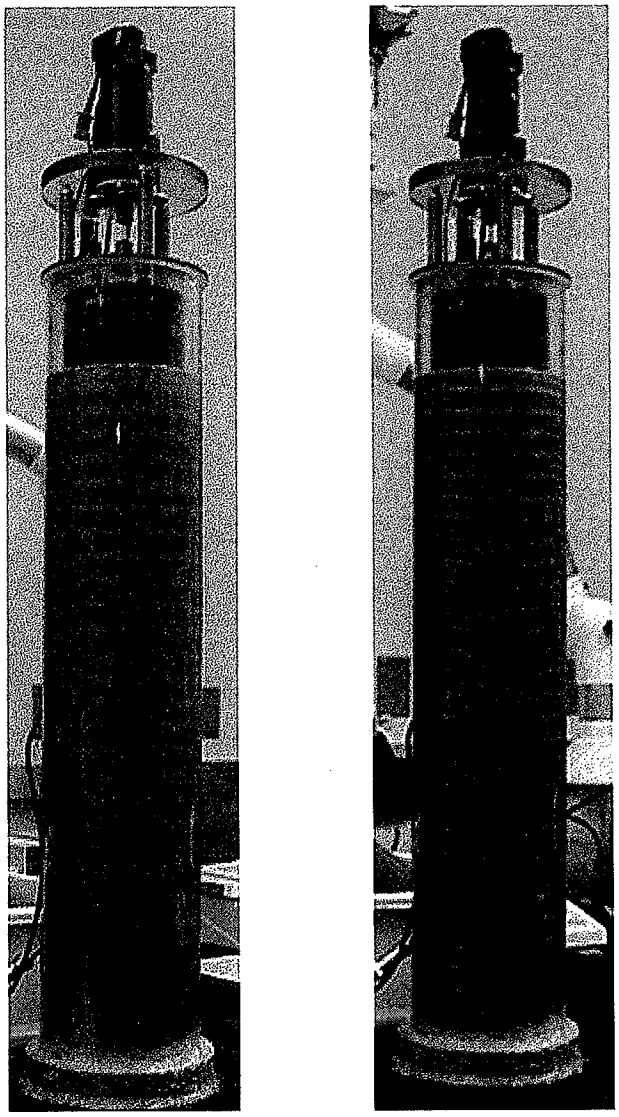

(a) (b)

FIG. B.5. Supercritical flow using Solution # 3 (composition 50:50 glycerol:water, by volume) and the large inner cylinder (a1 = 4.44 cm). (a) Taylor vortices; (b) wavy Taylor vortices.

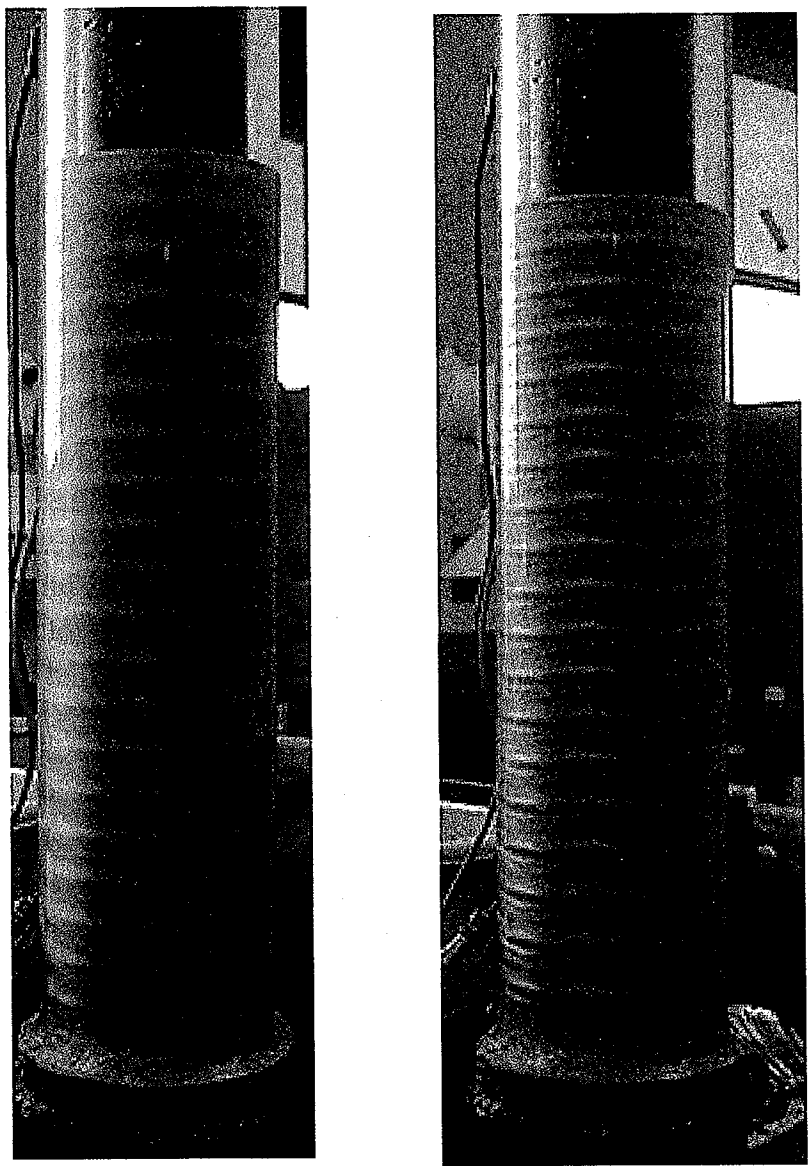

(a) (b)

FIG. B.4. Supercritical flow using Solution # 2 (composition 50:50 glycerol:water, by mass) and the small inner cylinder (a1 = 4.22 cm). (a) Taylor vortices; (b) wavy Taylor vortices.

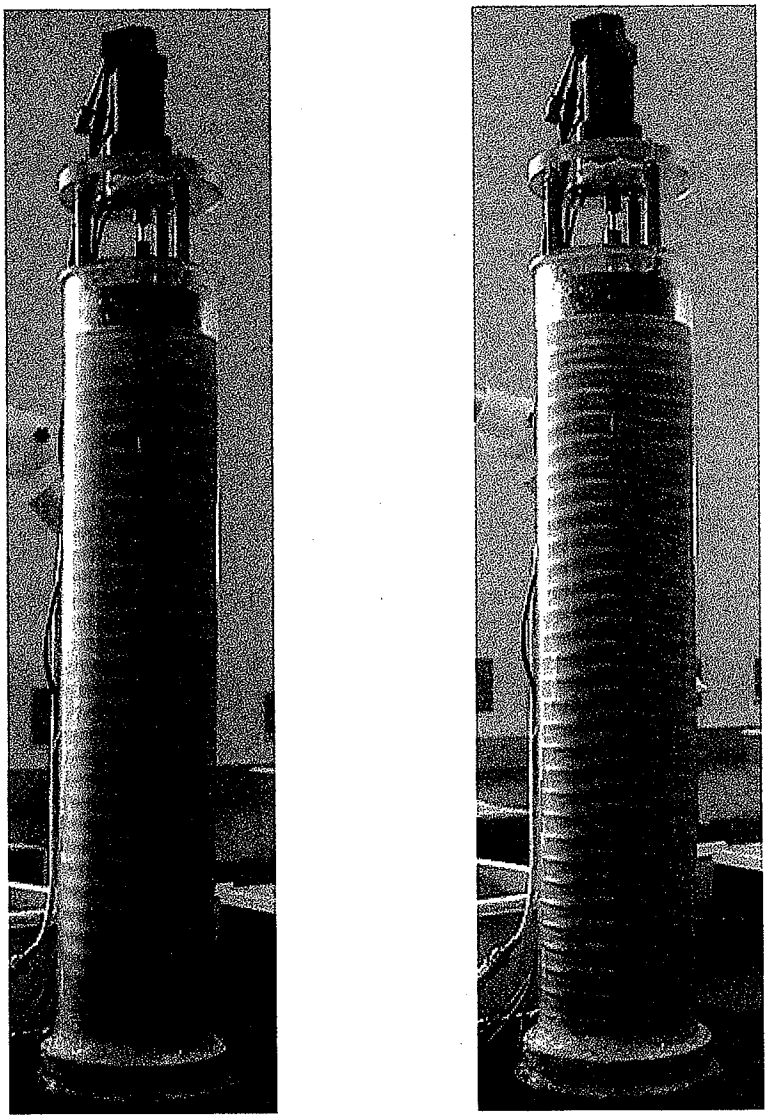

(a) (b)

FIG. B.3. Supercritical flow using Solution # 2 (composition 50:50 glycerol:water, by mass) and the large inner cylinder (a1 = 4.44 cm). (a) Taylor vortices; (b) wavy Taylor vortices.

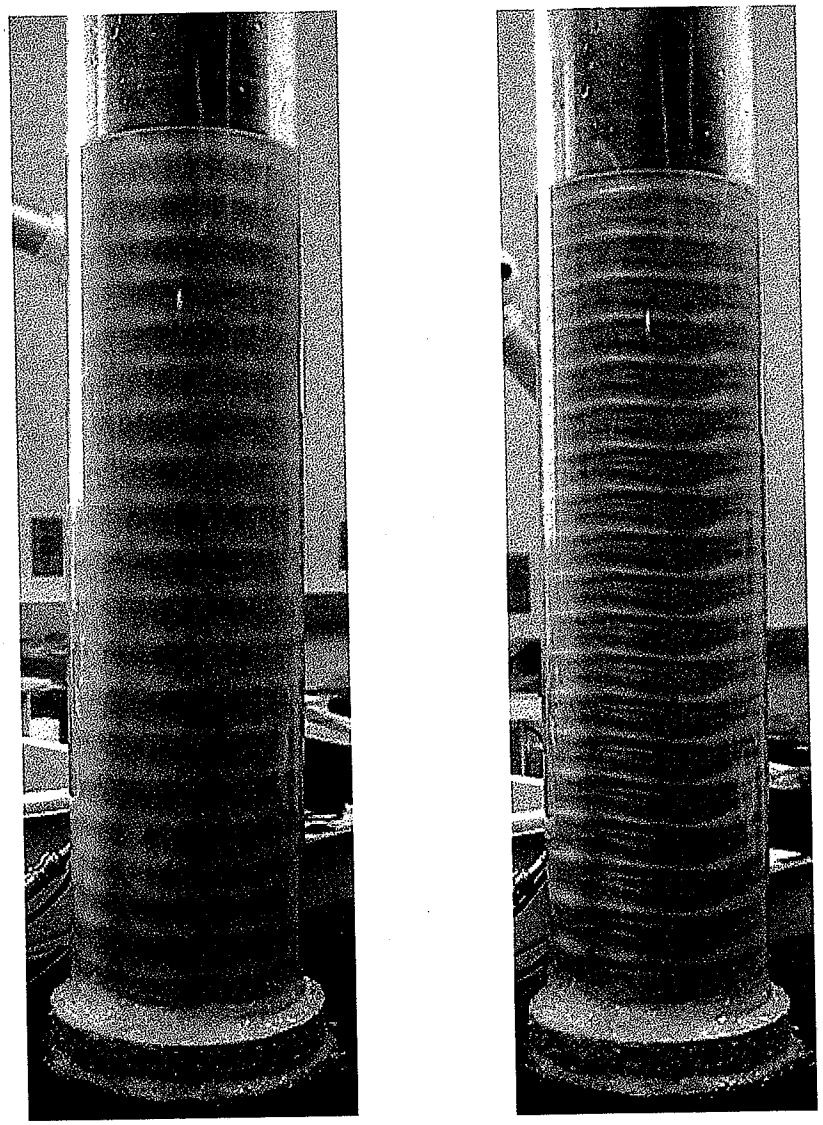

(a) (b)

FIG. B.2. Supercritical flow using Solution # 1 (composition 40:60 glycerol:water, by mass) and the small inner cylinder (a1 = 4.22 cm). (a) Taylor vortices; (b) wavy Taylor vortices.

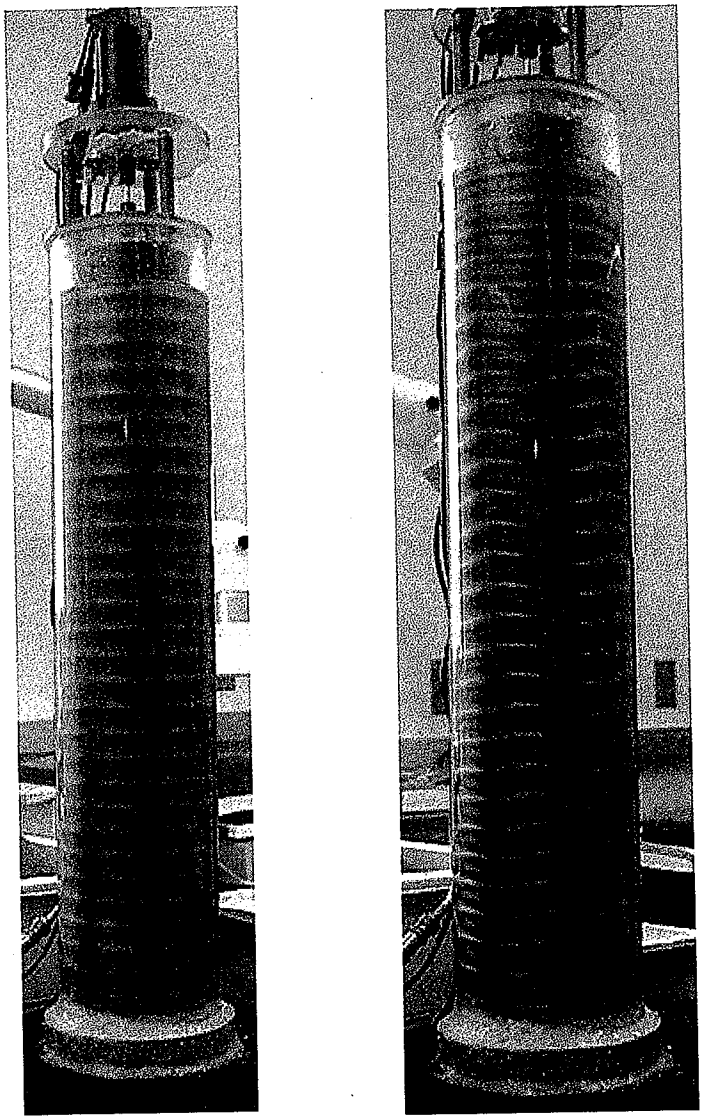

(a) (b)

FIG. B.1. Supercritical flow using Solution # 1 (composition 40:60 glycerol:water, by mass) and the large inner cylinder (a1 = 4.44 cm). (a) Taylor vortices; (b) wavy Taylor vortices.